Iba1+ Microglia Colocalize with *Synaptophysin+* and *Homer1+* Puncta and Reveal Two Novel Sub-types of GABAergic Neuron in Guinea Pig Inferior Colliculus

Author names and affiliations

Samuel David Webb[*] and Llwyd David Orton[*#]

[*] School of Healthcare Science, Manchester Metropolitan University, Manchester, M1 5GD

[#] Institute of Neuroscience, Newcastle University, Newcastle upon Tyne, NE2 4HH, UK

Corresponding and submitting author

Llwyd Orton

l.orton@mmu.ac.uk

+44 161 247 2483

School of Healthcare Science, Manchester Metropolitan University, Manchester, M1 5GD

Contributions (CRediT)

SW: Formal analysis, Investigation, Methodology, Validation, Visualization, Writing – original draft, review and editing.

LDO: Conceptualization, Data curation, Formal analysis, Funding acquisition, Methodology, Project administration, Resources, Supervision, Validation, Visualization, Writing – original draft, review and editing.

Conflict of interest

The authors declare no competing financial interests.

Acknowledgements

We thank Adrian Rees for generous donation of tissues and Claudia Racca for comments on an earlier version of the manuscript.

Abstract

Microglia have classically been viewed as the endogenous phagocytes of the brain, however, emerging evidence suggests roles for microglia in the healthy, mature nervous system. We know little of the contribution microglia make to ongoing processing in sensory systems. To explore *Iba1+* microglial structural and synaptic diversity, we employed the inferior colliculi as model nuclei, as they are characterized by sub-regions specialized for differing aspects of auditory processing. We discovered extensive *Iba1+* ramifications interacting with *homer1+* and *synaptophysin+* puncta (putative synapses) throughout the parenchyma. There was a greater density of these puncta in dorsal cortex, a sub-region specialized for mediating top-down corticofugal plasticity, than other sub-regions more specialized for processing ascending auditory or polymodal information. Cluster analyses revealed two novel sub-types of *GAD67+* neurons which can be distinguished solely based on the quantity of axo-somatic *Iba1+* contacts they receive. These data demonstrate *Iba1+* microglia exhibit specialized synaptic and cellular adaptations to ongoing processing in the mature, healthy auditory system. These specializations appear to relate to the afferent drive, plastic nature and inhibitory basis of local processing. Taken together, these findings suggest significant heterogeneity amongst microglia in sensory systems, related to the functional demands of their spatial niche.

Introduction

Inhibition is an essential element of neural processing and a defining component of sensory systems. GABAergic inhibition is prevalent in the auditory system, particularly in the principal auditory midbrain nuclei, the inferior colliculi (IC). Around a quarter of neurons in IC are GABAergic (Merchán et al., 2005), which may be why the IC is the most metabolically active nucleus in the mammalian brain (Sokoloff et al., 1977). Understanding how inhibitory cell types vary in different brain regions, to specialize for distinct functions, is a key area of neuroscientific study (Freund and Buzsaki, 1996; Tremblay et al., 2016). Most investigations into sub-types of inhibitory neurons naturally focus on the cells *per se*, including their morphology, electrophysiological firing characteristics, expression of cytoplasmic calcium binding proteins and peptides and RNA transcriptome. Another approach is to characterize and classify GABAergic neurons based on differences in the afferent axo-somatic inputs they receive (Ito et al., 2009; Beebe et al., 2016).

The IC has a tonotopic topography that can be divided into sub-regions. The central nucleus (CNIC) is dominated by neurons sharply tuned to simple auditory stimuli. The dorsal cortex (DCIC) has much broader frequency tuning and receives extensive corticofugal input and is specialized for synaptic plasticity (Herbert et al., 1991; Winer et al., 1998; Bajo and Moore, 2005; Bajo et al., 2010). The other major sub-region is the lateral cortex (LCIC) which exhibits polysensory tuning (Aitkin et al., 1978). These sub-regions are analogous to the core, belt and para-belt sub-regions found throughout the auditory pathway (Kaas and Hackett, 1999). Despite the essential role of the IC in hearing, little is known of how glial cells contribute to processing therein.

In addition to their neuroprotective and phagocytic functions, microglia contribute to ongoing synaptic function by removing unwanted structures in a process termed 'synaptic stripping' (Trapp et al., 2007). Furthermore, microglia interact with neurons during 'normal' processing and can sense and respond to local chemical signaling (Pocock and Kettenmann, 2007; Wake et al., 2009; Schafer et al., 2012). Certainly there is evidence for an active microglial influence on synaptic plasticity (Zhang et al., 2014; Riazi et al., 2015), but the nature of this role remains poorly understood.

Here, we take advantage of the functional organization of IC sub-nuclei to interrogate the anatomical inter-relationships of microglia, astrocytes, *GAD67+* (putative GABAergic) neurons

and *homer1+* (putative excitatory) synapses in guinea pig. Employing extensive multi-channel fluorescence immunohistochemistry and confocal microscopy, we show, for the first time, that *Iba1+* microglia, but not *GFAP+* astrocytes tile the IC parenchyma. Furthermore, *Iba1+* processes colocalize with *synaptophysin+* and *homer1+* puncta, demonstrating localization with putative metabotropic glutamate receptors. These puncta vary between sub-regions with greater numbers in DCIC, suggesting a role for *Iba1+* microglia in corticofugal plasticity. Multivariate statistical approaches revealed two novel types of *GAD67+* neuron that can be perfectly discriminated based on the quantity of *Iba1+* processes abutting their soma. Our findings open new avenues to explore the fundamental yet under-investigated role microglia play in ongoing processing in mature nervous systems.

Materials and methods

Regulation and Ethics

All animals were housed and procedures performed in accordance with the terms and conditions of a license (PPL 60/3934) issued by the UK Home Office under the Animals (Scientific Procedures) Act 1986. Ethical approval was provided by the Local Ethical Review committee at Newcastle University and the School of Healthcare Science Ethics Committee at Manchester Metropolitan University.

Animals

Results are described from four adult (one at four months old, three at six months old) outbred, tricolor guinea pigs (*Cavia porcellus*) of both sexes (three male, one female). Animal weights on the morning of each respective perfusion ranged from 675g to 867g. We aimed to minimize the number of animals used and their suffering at all times.

Anesthesia and Tissue Processing

Animals were deeply anesthetized with sodium pentobarbital (i.p. injection; Euthanal, Merial; 200mg/ml, 2 ml volume). After five minutes, the pedal withdrawal and blink reflexes were assessed to confirm a deep plane of anesthesia. This was followed by transcardial gravity perfusion with 500mls of 0.1M heparinized PBS followed by 500mls of freshly made 4% paraformaldehyde in 0.1M PBS. Both solutions were pH 7.2 directly prior to use.

Brains were removed with rongeurs (Micro Friedman, 0.8mm jaws, WPI) and post-fixed in 30% sucrose in 4% paraformaldehyde, for at least 3 days at 4°C. Once brains sank, they were cut in the coronal plane with a razor blade through the parietal and temporal lobes, at around the rostro-caudal location of the medial geniculate. The tissue block was then placed in an embedding mold (Peel-a-way; Shandon), covered in embedding medium (OCT; Agar Scientific) and frozen at -80°C. 60µm sections were taken on a cryostat (HM560, Microm) and collected in 12 well plates in cryoprotectant (30% sucrose, 30% ethylene glycol, 1% polyvinyl pyrrolidone-40 in 0.1M PBS) and stored at -20°C until use (Watson et al., 1986; Olthof et al., 2019).

Antibody characterization

The following primary antibodies were used:

Mouse anti-GAD67 (1:500; monoclonal; clone 1G10.2; MAB5406; lot# 2636700; Millipore; RRID: AB_2278725) – according to the manufacturer, the immunizing antigen is a recombinant fusion

protein containing unique N-terminus regions from amino acids 1-101 of *GAD67*. Immunoblotting detects a 67kDa protein in rat cerebellum and mouse microsomes; immunohistochemistry demonstrated labelling similar in distribution to *in situ* mRNA hybridization (Fong et al., 2005; Kotti et al., 2006; Ramirez et al., 2008). Use of this antibody has been published in guinea pig IC (Nakamoto et al., 2013; Foster et al., 2014; Beebe et al., 2016), as well as rat IC (Ito et al., 2009).

Mouse anti-GFAP (1:500; monoclonal; clone G-A-5; G3893; lot# 045M4889V; Sigma; RRID: AB_477010) – according to the manufacturer, this antibody is raised against an epitope from the C-terminus of *GFAP* in purified pig spinal cord (Latov et al., 1979; Debus et al., 1983). The antibody has been shown to recognize a single band of approximately 50kDa and reacts with homologous, conserved residues across mammals (Lorenz et al., 2005). The use of this antibody has been demonstrated in many species, including mouse (Komitova et al., 2005), rat (Lennerz et al., 2008; Sanchez et al., 2009), tree shrew (Knabe et al., 2008), guinea pig (Kelleher et al., 2011; Kelleher et al., 2013) and human (Toro et al., 2006). Labelling observed in this study was consistent with these studies and the known morphology of astrocytes.

Rabbit anti-calbindin D-28k (1:1,000; polyclonal; AB1778; lot# 2895780; Millipore; RRID: AB_2068336) – according to the manufacturer, this antibody recognizes a single band at 28kDa in human, mouse, and rat brain tissues. It does not bind to calretinin and pre-adsorbtion of diluted antiserum with calbindin removed all labelling in human brain (Huynh et al., 2000). Previous labelling of mouse olfactory bulb (Kotani et al., 2010), rat piriform cortex (Gavrilovici et al., 2010) and guinea pig enteric nervous system (Liu et al., 2005) all showed highly selective cytoplasmic labelling of neurons. We observed labelling consistent with previous reports.

Rabbit anti-calretinin (1:1,000; polyclonal; AB5054; lot# 2903043; Millipore; RRID: AB_2068506) – according to the manufacturer, this antibody recognizes the 29kDa protein in mouse and rat tissues (Su et al., 2010; Yanpallewar et al., 2010). This highly conserved epitope has also been labelled in hamster (Lee et al., 2004), zebrafish (Goodings et al., 2017) and turtle (Parks et al., 2017). We observed labelling consistent with these previous reports.

Rabbit anti-Iba1 (1:1,000; polyclonal; 019-19741; lot# WDE1198; Wako; RRID: AB_839504) – according to the manufacturer, this affinity purified antibody was raised against a synthetic peptide corresponding to the C-terminus fragment of rat *Iba1*. Labelling via western blot was positive for a 17kDa band (Imai et al., 1996). We observed selective labelling of ramified

145 microglia, matching similar reports in mouse (Bulloch et al., 2008), rat (Helfer et al., 2009;
146 Fuentes-Santamaría et al., 2012), Japanese quail (Mouriec and Balthazart, 2013), macaque
147 (Stanton et al., 2015) and chimpanzee (Rosen et al., 2008). We observed labelling consistent
148 with these previous reports.
149 *Mouse anti-synaptophysin* (1:500; monoclonal; S5768; lot# 103M4778; Sigma; RRID:
150 AB_477523) – according to the manufacturer, this antibody targets a pre-synaptic
151 synaptosome antigen derived from rat retina, producing a 38kDa band in rat brain extracts.
152 We observed punctate labelling, as previously reported in mouse (Wiedenmann and Franke,
153 1985), rat (Zelano et al., 2009), guinea pig (Glueckert et al., 2008), and human (Jaafari et al.,
154 2008).
155 *Chicken anti-homer1* (1:500; polyclonal; 160026; lot# Q86YM7-1; SySy; RRID: AB_2631222) –
156 according to the manufacturer, this IgY antibody is specific for residues 1-196 of human
157 *homer1*, including splice variants a-d (Soloviev et al., 2000). These residues are highly
158 conserved, with reactivity for mouse and rat. *Homer1* has been shown to selectively bind to
159 glutamate receptors (Brakeman et al., 1997) and can be considered a marker of glutamatergic
160 synapses when colocalized with synaptophysin (Ciruela et al., 2000; Sala et al., 2001; Lee et al.,
161 2019). This antibody has recently been validated in mouse models of Alzheimer's disease via
162 colocalization with *synaptophysin* (Reichenbach et al., 2018).
163 Blood vessels were labelled with rhodamine conjugated Griffonia (Bandeiraea) Simplicifolia
164 Lectin 1 (1:100; RL-1102; Vector; lot# S0926RRID: AB_2336492), which binds to glycoproteins
165 lining the inner lumen.
166 *Fluorescence immunohistochemistry*
167 Sections through the superior colliculus and the rostral-most third along the rostro-caudal axis
168 through the IC were first used to optimize labelling. Data are presented from sections in the
169 middle third of the IC along the rostro-caudal axis, which contained the CNIC, DCIC and LCIC.
170 The location of each section through the rostro-caudal axis was referenced to an atlas of the
171 guinea pig brainstem (Voitenko and Marlinsky, 1993).
172 All steps in the labelling protocol involved continuous gentle agitation of sections. Free-
173 floating sections were brought to room temperature and washed 3x5mins in PBS. Sections
174 were blocked and permeabilized in 5% normal goat serum (Vector) and 0.05% Triton X-100
175 (Sigma) in PBS for one hour. Following blocking, a cocktail of primary antibodies was added

to the blocking solution and applied to sections overnight at room temperature. The next day, sections were washed 3x5mins in PBS and incubated for two hours in appropriate secondary antibodies (Invitrogen; 1:250 in blocking solution). For double labelling of *Iba1* and *GAD67*, goat anti-rabbit AlexaFluor 488 and goat anti-mouse AlexaFluor 568 were used. For double labelling of calbindin and *GFAP*, goat anti-rabbit AlexaFluor 488 and goat anti-mouse AlexaFluor 647 were used. For triple labelling of *Iba1*, *GSL1* (pre-conjugated rhodamine fluorophore) and *GFAP*, goat anti-rabbit AlexaFluor 488 and goat anti-mouse AlexaFluor 647 were used. For triple labelling of *Iba1*, *homer1* and *synaptophysin*, goat anti-rabbit AlexaFluor 405, goat anti-chicken AlexaFluor 568 and goat anti-mouse AlexaFluor 647 were used. Sections were then mounted on slides and coverslipped using Vectashield (Vector Labs, H-1000) and kept at 4°C until imaged. All experiments had control slides where the primary, secondary or both the primary and secondary antibodies were excluded. This allowed detection of autofluoresence and any aspecific signal and ensured only signals from primary and secondary binding to targets were imaged.

Image acquisition

Sequentially acquired micrographs were taken with a confocal microscope (Leica SP5) using a wide field stage and zoom function. Images were acquired via a 40x objective for images of the entire cross-section of the IC, and a 63x objective for region of interest (ROI) panoramas and high magnification images. Whole IC images were taken using 5µm equidistant slices in the Z-plane to produce maximum intensity tiled projections. For *GAD67* and *Iba1* ROI panoramas, 6-column x 5-row tiled images were taken using 0.99µm z-slices and rendered as maximum intensity projections. High magnification images of *Iba1* and synaptic marker labelling were imaged using 0.05µm z-slices through the full cell.

Image analyses

For *Iba1+* cell density estimates, tiled panorama images of the IC were subject to manual cell counts. The peripheral borders of the IC were delineated and a contour drawn, and each image cropped to its respective contour. To make fair comparisons between cases, 450µm^2 grids were placed across each IC panorama image and centered on the middle pixels of each micrograph in ImageJ. Only those grids which were filled entirely by stained parenchymal tissue were subject to counts. Comparisons were then made between cases, such that only grids that were

present in images from all four animals were included in calculation of group means and standard deviations per grid.

Maximum intensity projection ROI panoramas were analyzed for i) cell counts, ii) percentage field of view covered analyses, iii) individual *Iba1+* cell Sholl and iv) skeleton analyses using Fiji ImageJ (Abràmoff et al., 2004). All panorama micrographs were first processed by filtering monochrome images using a median pixel (1.5) filter and then thresholded to binary by implementing the IsoData algorithm. Cell counts, and percentage field of view covered analyses were then performed using the Analyze Particles plugin. For Sholl analyses, individual *Iba1+* microglia were cropped and a series of equidistant radiating 1µm concentric circles were plotted from the center of the cell body to the furthest radiating extent of ramification. Each intersection with a concentric ring was measured. The Skeletonize algorithm was used to display a one-pixel thick framework of each microglial cell. The Analyze Skeleton plugin calculated number of branches and branch lengths for each cell. Whole IC images of *synaptophysin* were analyzed for labelling (pixel intensity) density between sub-regions using the Measure function.

To measure *Iba1+* putative-interactions with *GAD67+* neurons, individual cells were cropped from panoramas, and were measured without filtering. The diameter of *GAD67+* somata were quantified by measuring the extremes of each *GAD67+* cell in the z-plane. Only cells that were entirely contained within the full z-range of the section were included. All other measures of putative interactions between *Iba1+* and *GAD67+* labelling were subject to extensive manual counts on a slice-by-slice basis through each z-stack.

For synaptic colocalization measurements, z-slices through *Iba1+* microglia were thresholded using the Itso algorithm to develop a mask of each slice of the cell and then converted into a stack. Synaptic marker labelling (*synaptophysin* and *homer1*) were thresholded using the Moments algorithm to create masks of each slice. To enable comparison of putative excitatory synapses, monochrome image slices of *synaptophysin* were merged with *homer1+* labelling. These stacks were then respectively merged with the masks of the *Iba1+* masked stack, enabling visualization of co-localization between putative excitatory synapses and microglial processes. A 3D Sholl analysis of volume was then conducted using concentric rings of 0.025µm from the center of each *Iba1+* soma, which gave a quantitative measurement of co-

localization across the x, y, and z planes. Each point of colocalization detected was visually inspected and verified before being included in the dataset.

Statistical analysis

Data were collected in Excel spreadsheets. Statistical hypothesis testing was performed in Prism 7 (GraphPad). Factorial analyses were conducted using the non-parametric Kruskall-Wallis ANOVA with sub-region as the factor in all cases. Where appropriate, *post-hoc* tests with Dunn's method were conducted. For *post-hoc* analyses the α was Šidák corrected for multiple comparisons. Spearman's rank correlations were used to investigate potential associations between dependent variables.

Principal component, two-step cluster and K-means squared cluster analyses were conducted in SPSS v25 (IBM). The exploratory two-step cluster analysis employed Euclidean distance measures with Schwarz's Bayesian clustering criterion. The K-means clustering analysis had 10 maximum iterations and classified data into one of the two identified clusters. All 160 cell ROIs were successfully classified by this analysis. All reported P values are exact and two tailed.

Results

GFAP+ astrocytes and Iba1+ microglia form the glia limitans externa and neurovascular unit in IC

We first sought to identify the distribution of *GFAP+* astrocytes and *Iba1+* microglia in adult guinea pig IC. Coronal, 60µm sections showed pronounced *GFAP+* and *Iba1+* labelling of the *glia limitans externa* lining the dorsal and lateral borders of the IC (Figure 1A). Extensive labelling was also distributed medially, lining the cerebral aqueduct, with ramified *GFAP+* astrocytic processes radiating into the periaqueductal grey, as well as the commissure of the IC. Interestingly, we found no *GFAP+* astrocytes throughout the IC parenchyma, save for sparse labelling of cells in the outermost layers of the DCIC and LCIC. Conversely, ramified *Iba1+* microglia tiled the parenchyma in non-overlapping domains with similar density throughout the IC, as quantified in Figure 1B.

Combining *Iba1* and *GFAP* labelling with the fluorescent-conjugated lectin *GSL1* revealed extensive *peri*-vascular labelling along putative penetrating arteries and arterioles (Figure 1C). Neurons expressing cytoplasmic calbindin or calretinin were distributed in the outermost regions of the cortices of the IC, matching previous reports (Zettel et al., 1997; Ouda et al., 2012) and in close proximity to vessels and *GFAP+* processes (Figure 1D).

These findings demonstrate that many aspects of IC glial organization mirror those reported in other brain regions, with both *GFAP+* astrocytes and *Iba1+* microglia forming the *glia limitans externa* and lining adjacent to blood vessels. However, the observation that *Iba1+* microglia but not *GFAP+* astrocytes were found throughout the parenchyma, suggests a role for *Iba1+* microglia in glial-neuronal putative interactions in IC.

Distributions of Iba1+ microglia and GAD67+ somata vary between sub-regions of IC

To explore the role of parenchymal microglia in IC, we acquired tiled confocal micrographs of *Iba1+* microglia (Figure 2A) and *GAD67+* neurons (Figure 2B) across whole coronal IC sections (Figure 2C). Labelling revealed putative GABAergic neurons throughout the IC, with increased cell density in high-frequency ventral regions, matching previous reports (Ito et al., 2009; Gleich et al., 2014; Beebe et al., 2016). Dividing the IC into sub-regions based on the criteria of Coote and Rees (2008) allowed definition of ROIs for comparisons between DCIC, LCIC, mid-CNIC and ventral-CNIC (VCNIC), respectively (Figure 2D). Cell counts confirmed a greater number of *GAD67+* neurons in VCNIC (Figure 2E) ($H(3)=24.42$; $p<0.001$) than other sub-

regions (*post-hoc* Dunn's tests: VCNIC vs DCIC $p<0.0001$; VCNIC vs LCIC $p=0.0023$). Mid-CNIC also had a greater number of *GAD67+* neurons than DCIC ($p=0.026$) and LCIC ($p=0.395$).

Analyses of ROIs confirmed similar densities of *Iba1+* microglia cell counts between sub-regions of IC, in spite of the varying density of *GAD67+* cells (Figure 3). The DCIC had slightly more densely packed *Iba1+* microglia than other sub-regions, with a median of 88 cells (range=70 to 106) per 432x552µm ROI. Mid-CNIC had a median of 83 (range=76 to 95), while LCIC had a median of 80 (range=63 to 104) and VCNIC had a median of 73 (range=57 to 92). However, a Kruskall-Wallis ANOVA with sub-region as the factor found no detectible difference between groups ($H(3)=4.91$, $p=0.179$).

Contrastingly, the percentage field of view of *Iba1+* labelling (above a thresholded binary level, consistent between cases) was much greater in DCIC (median=14.8%; range=8.7 to 22.5) than mid-CNIC (9.5%; 7.1-13.9), LCIC (8.9% 4.9-12.4) or VCNIC (7.4%; 4.3-12.0). These differences between groups are likely a real effect ($H(3)=12.67$; $p=0.0034$; *post-hoc* Dunn's test between DCIC and VCNIC $p=0.002$). The greater amount of *Iba1+* labelling in DCIC, despite similar soma density between sub-regions, suggests differences in other aspects of *Iba1+* microglia morphology.

Iba1+ microglia in DCIC are more ramified than other sub-regions of IC

We predicted that the stronger *Iba1+* microglia labelling in DCIC neuropil was primarily due to a greater number and extent of ramifications compared to other sub-regions of IC. To test this, we conducted Sholl analyses for a total of 40 cells per sub-region (n=160). The maximum intensity projection of each *Iba1+* microglial cell was imaged and analyzed in x and y dimensions.

Cells were identified and selected from ROI images (Figure 4A&B). Background/non-cellular labelling was cropped (Figure 4C) and cellular labelling thresholded to generate binary images (Figure 4D). The number of intersections at every micrometer distance from the center of the soma was calculated (Figure 4E). Binary thresholded cells were also skeletonized to derive information about the shape and structure of ramifications, such as the number of branches and maximum branch length (Figure 4F).

Iba1+ microglia were more ramified in DCIC than mid-CNIC, LCIC or VCNIC at all distances away from the soma (Figure 5A). The total number of intersections of every ramification, across cells (independent of distance from the soma) had a median value of 438 in DCIC (IQR=385 to

500). This was greater than in mid-CNIC (332; ±284-399), LCIC (363; ±326-422), or VCNIC (353; ±302-400) (Figure 5B). A Kruskal-Wallis one-way ANOVA on ranks, with sub-region as the factor found the differences between sub-regions of IC were likely a real effect ($H(3)=54.36$; $p<0.0001$). *Post-hoc* analyses via Dunn's tests showed differences between DCIC and the other three sub-regions were likely to be a real effect (all $p<0.0001$).

Analyses of skeletonized *Iba1+* microglia revealed those in DCIC also had a greater number of branches (Figure 5C), with a median of 269 (±222-312). This was greater than mid-CNIC (183; ±150-229), LCIC (193; ±165-224), and VCNIC (165; ±138-201). These differences were also likely a real effect ($H(3)=71.30$, $p<0.0001$; Dunn's tests DCIC vs other sub-regions all $p<0.0001$). Conversely, maximum branch length, defined as the longest distance covered by any ramification of skeletonized *Iba1+* microglia without branching, followed the opposite trend. Longest distances were found in VCNIC (median=14.44µm; IQR=12.76-17.18) (Figure 5D). Shorter distances were found in LCIC (14.01; IQR±=11.92-16.16), mid-CNIC (12.86; ±11.22-15.60) and DCIC (11.62; ±11.26-15.01). The difference between VCNIC and DCIC was likely a real effect ($H(3) =12.18$, $P = 0.0068$; *post-hoc* Dunn's test $p=0.0079$).

Iba1+ putative interactions reveal two novel types of GAD67+ neurons in IC

We hypothesized that *GAD67+* neurons, which are known to receive a variety of types of presynaptic contacts (Ito et al., 2009; Beebe et al., 2016), may also receive different types of *Iba1+* inputs. To examine the nature of *Iba1+* putative interactions with *GAD67+* neurons, we quantified five dependent variables from each cell ROI (n=160): (i) *GAD67+* soma maximum diameter; (ii) percentage of *GAD67+* soma abutted by *Iba1+* processes; (iii) number of *Iba1+* microglia with processes abutting each *GAD67+* soma; (iv) number of distinct *Iba1+* processes abutting each *GAD67+* soma; and (v) total length of *Iba1+* processes abutting each *GAD67+* soma (µm). These features were calculated from micrographs such as the representative example in Figure 6A, which shows a *GAD67+* neuron being abutted by two *Iba1+* microglia.

A correlation matrix revealed weak associations between *GAD67+* soma maximum diameter (i) and the other four dependent variables (ii-v) (Figure 6B). There were stronger correlations between the four *Iba1* related variables (ii-v). As these variables were only weakly correlated with *GAD67+* neuron diameter, we further investigated whether a multivariate analysis could better explain the observed distributions.

We conducted an exploratory two-step cluster analysis including all five variables. We employed Euclidean distance measures with Schwarz's Bayesian clustering criterion. The model found two clusters with good silhouette measures of cohesion and separation (~0.7), suggesting good explanatory power. We then conducted a principal component analysis for the five variables across all cells in all sub-regions of the IC. The data showed a clear dissociation between *GAD67+* neuron diameter in one cluster and the other four variables, which clustered together (Figure 6C). Both clusters were categorized using a standard correlation coefficient of >0.5 as a cut-off value, which showed one cluster was explained by only the *GAD67+* neuron diameter variable, while the other cluster had significant contributions from all four of the *Iba1+* related variables. These trends were also true for all sub-region analyses in IC (Figure 6Di-iv).

We conducted a K-means squared cluster analysis with 10 maximum iterations, which classified data into two clusters. All 160 cell ROIs were classified by this analysis. There were 42 cases in cluster 1, and 118 in cluster 2. To visualize the contribution of each of the four *Iba1* related variables, each was plotted as a function of *GAD67+* neuron diameter (Figure 7A-D). These scatterplots revealed a dissociation with little overlap between the two clusters using the percentage *Iba1+* coverage onto *GAD67+* somata (Figure 7A). There was perfect discrimination between the clusters using a cut-off value of 0.28 of the normalized total µms of *Iba1+* putative interactions with *GAD67+* neuron somata (Figure 7B). The cut-off line (grey dash) was perpendicular to the *GAD67+* neuron diameter axis, showing that this value was independent of *GAD67+* soma diameter. Conversely, the number of *Iba1+* cells contacting each *GAD67+* soma had a significant degree of overlap with little difference between clusters (Figure 7C). The number of *Iba1+* processes abutting *GAD67+* somata had little overlap between distributions (Figure 7D).

To compare the ability of each of these variables to independently discriminate between the two clusters, we conducted ROC analyses (Figure 7E). These data revealed that while each variable had an area under the curve >0.5, the three variables relating to the nature of *Iba1+* processes abutting *GAD67+* neurons had the best discriminatory power.

Iba1+ putative interactions with GAD67+ neurons show little difference between sub-regions of IC

We explored whether any of the variables or clusters identified had a relationship to the sub-region of IC in which the cells were located. Diameter of *GAD67+* somata did not vary between sub-regions (Figure 8A) ($H(3)=5.3$; $p=0.151$). A small difference was found for the percentage of *GAD67+* soma covered by *Iba1+* processes (Figure 8B) ($H(3)=9.9$; $p=0.019$). *Post-hoc* Dunn's tests suggested a potential real difference between DCIC and VCNIC ($p=0.012$). However, there was extensive overlap between the distributions so there is a reasonable chance this may not be a true effect. The number of *Iba1+* cells abutting each *GAD67+* somata (Figure 8C) ($H(3)=6.44$; $p=0.092$), the number of *Iba1+* contacts onto *GAD67+* somata (Figure 8D) ($H(3)=5.55$; $p=0.141$), and the normalized total number of µm covered by *Iba1+* contacts onto *GAD67+* somata (Figure 8E) ($H(3)=4.64$; $p=0.200$) did not differ between sub-regions. However, the number of *GAD67+* cells contacted by each *Iba1+* cell was greater in VNCIC (Figure 8F) ($H(3)=21.32$; $p=0.0006$). *Post-hoc* Dunn's tests revealed a likely real difference between VNCIC and DCIC ($p=0.005$). We interpret this as being due to the greater density of *GAD67+* neurons in VCNIC (Figure 2E).

Both clusters had a similar proportion of ROIs from each of the four sub-regions of IC (cluster 1: 10 DCIC (24%), 14 mid-CNIC (33%), 13 LCIC (31%), 5 VCNIC (12%); cluster 2: 30 DCIC (25%), 26 mid-CNIC (22%), 27 LCIC (23%), 35 VCNIC (30%)).

Iba1+ microglial processes colocalize at puncta with synaptophysin and homer1 in greater numbers in DCIC

To determine whether *Iba1+* processes are present at synapses in IC, *Iba1* was co-labelled with the pre-synaptic marker *synaptophysin* and a marker of glutamatergic post-synapses, *homer1*. Figure 9A shows a tiled confocal micrograph of *synaptophysin* (magenta) and *Iba1* (green) labelling. A clear shift in *synaptophysin* density can be seen from DCIC to CNIC. Quantification from ROIs in each sub-region confirmed *synaptophysin* was more densely distributed in DCIC than other sub-regions and mirrored the distributions of *Iba1+* percentage field of view (Figure 9B). Note that these percentage field of view values are calculated from different ROIs than the analyses presented earlier.

To examine the cellular location of these puncta on *Iba1+* microglia, we imaged three cells in each sub-region in very fine z-slice steps (0.05µm). A representative image of one z-plane

401 through an *Iba1+* microglial cell in VCNIC is shown in Figure 10A-D, showing a point of
402 colocalization between *synaptophysin*, *Iba1,* and *homer1* (arrowhead). A rectangular ROI was
403 drawn around colocalized pixels of approximately 0.5μm^2. Plotting spectrographs of pixel
404 intensity for pairwise combination of each of the three labels showed positive relationships
405 (Figure 10E-G), with colocalization rates ranging from 76.5% to 95.0%. 3D reconstructions of
406 *Iba1+* microglia, including all ramifications (Figure 10H, green), and points of colocalization
407 with *synaptophysin* and *homer1* (Figure 10H, magenta), allowed visualization of the locations
408 of these markers.
409 We conducted 3D volume Sholl analyses (Figure 11A) which revealed *Iba1+* microglia in DCIC
410 had a greater number of colocalized puncta. Fitting each sub-region with a LOWESS regression
411 revealed this trend occurred at all distances from the soma. Quantification of total number of
412 puncta per cell in each sub-region showed that DCIC had a greater number than other sub-
413 regions (Figure 11B). We also determined the location of each puncta with respect to the
414 branching ramifications of each *Iba1+* cell. Puncta were classified as being located on the
415 soma, primary, secondary, tertiary or quaternary branches. Figure 11C shows that when
416 normalized, the relative proportion of puncta locations on *Iba1+* microglia was similar across
417 sub-regions (Table 1; χ^2=7.20; p=0.844).

Discussion

These findings reveal *Iba1+* microglia express morphologies and putative synaptic interactions commensurate with a functional role in activity dependent neurotransmission and synaptic plasticity in the healthy, mature auditory system. Our data show that *Iba1+* microglia ramifications, but not those of *GFAP+* astrocytes, interact with *homer1+* (putative glutamatergic) synapses in IC parenchyma. Taking advantage of the specialized and functionally diverse sub-regions of IC, we found the first evidence, to our knowledge, for a greater number of such synapses in DCIC, an area known to receive a greater proportion of glutamatergic corticofugal contacts, than other IC sub-regions. Cluster analyses revealed two new types of *GAD67+* neuron defined by the extent of *Iba1+* microglial contacts onto their soma. These data reshape our understanding of the role of microglia in 'normal' processing within sensory systems and propose hitherto unexplored avenues of investigation. Similar approaches in other brain areas may produce novel understandings of brain organization.

Significance of sub-regional differences

Some aspects of central sensory processing can be interpreted through triad models of organization. Such models are based on observations that central sub-regions of sensory pathways are dominated primarily by i) ascending innervation producing brisk responses at short latencies to simple stimuli. Located adjacent are at least two regions with longer response latencies - one of which typically receives ii) a diversity of polymodal inputs, while the other is iii) primarily driven by descending, top down afferents. In the somatosensory system, these have been respectively termed the lemniscal, para-lemniscal and extra-lemniscal pathways (Yu et al., 2006), while in the auditory system the terms core, belt and para-belt have been coined (Kaas and Hackett, 1999). These regions exhibit differing connectional as well as cytoarchitectonic and chemoarchitectonic organization (Sweet et al., 2005).

In IC, there is longstanding evidence for a triad model of organization using a diversity of methodologies. These include electrophysiology (Syka et al., 2000) , fMRI (Baumann et al., 2011; De Martino et al., 2013), histology (Faye-Lund and Osen, 1985), immunohistochemistry (Coote and Rees, 2008) and tract tracing of projections (for review of afferent and efferent inputs see Malmierca and Hackett (2010) and Schofield (2010)). The present study provides evidence that *Iba1+* microglial processes, despite superficially appearing similar throughout IC (Figure 1&3), also exhibit profound differences between sub-regions (Figure 5).

The greater density of *Iba1+* microglial processes at *synaptophysin+ and homer1+* synapses in DCIC has implications for auditory processing. Cortical regions of IC exhibit much stronger novelty detection and stimulus specific adaptation than CNIC (Ayala and Malmierca, 2013). This may partly relate to the primary afferent drive to DCIC being descending corticofugal fibers (Herbert et al., 1991; Winer et al., 1998; Bajo and Moore, 2005; Bajo et al., 2006). Projections to DCIC from auditory cortex originate from glutamatergic (Feliciano and Potashner, 1995) pyramidal cells in layer V (Games and Winer, 1988; Winer and Prieto, 2001). Corticofugal inputs to DCIC primarily target glutamatergic IC neurons (Nakamoto et al., 2013), while large *GAD67+* neurons in DCIC are a source of tectothalamic inhibition with shorter response latencies than other cells in DCIC (Geis and Borst, 2013). How the greater proportion of *Iba1+* synapses in DCIC influences auditory processing is unknown, but one might suggest on the basis of greater density of *synaptophysin* labelling in DCIC, that there are a greater number of synapses *per se*. Certainly the DCIC receives a greater diversity of inputs than CNIC, including from auditory cortex, the contralateral IC (Orton et al., 2016), and ascending projections from the brainstem. However, the highly plastic nature of synaptic processing in DCIC leads to the speculation that *Iba1+* microglial processes may actively contribute to and shape synaptic processing and plasticity therein. Evidence for microglial involvement in such processing has been described in other models, including synaptic stripping and removal of existing synapses (Trapp et al., 2007), or sensing neuronal synaptic activity (Pocock and Kettenmann, 2007) in an activity dependent manner (Wake et al., 2009; Tremblay et al., 2010). The latter may facilitate microglial influence over synaptic plasticity via modulation of glutamatergic (Hayashi et al., 2006) or purinergic (Tsuda et al., 2010) neurotransmission. Corticofugal inputs to DCIC have been shown to play an essential role in auditory learning and plastic reweighting of cues (Bajo et al., 2010; Keating et al., 2013). These connections likely underlie elements of human adaptation in unilateral hearing loss (Kumpik and King, 2019), though molecular mechanisms for these observations are underexplored. Intriguingly, *homer1* has recently been shown to mediate behavioral plasticity in association with metabotropic glutamatergic synaptic plasticity in hippocampus (Wagner et al., 2014; Clifton et al., 2017; Gimse et al., 2018). The presence of *Iba1+* processes at *homer1+* synapses suggests a microglial role in modulating synaptic function and plasticity in DCIC, potentially in a similar manner to that shown in other brain regions.

Two novel clusters of GABAergic neurons

As the auditory pathway contains a large proportion of inhibitory neurons, with around a quarter of neurons being GABAergic (Oliver et al., 1994; Merchán et al., 2005), understanding their structure, function, and organization is a fundamental question. Previous approaches to classifying *GAD67+* neurons in IC have focused on soma size (Roberts and Ribak, 1987a, 1987b; Ono et al., 2005) coupled with axo-somatic inputs (Ito et al., 2009), perineuronal nets (Beebe et al., 2016) or cytoplasmic calcium binding protein expression (Ouda and Syka, 2012; Engle et al., 2014). The present analyses show that while there is merit to these approaches, other features of GABAergic sub-types exist. Indeed, we have discovered that *GAD67+* cells can be classified into two distinct clusters based on the total amount of *Iba1+* contacts onto their soma (Figure 7). That GABAergic neurons in IC can be defined based on *Iba1+* inputs suggests that microglia are essential to the structure and function of IC processing in the mature, adult auditory system.

ROC analyses revealed that the two clusters could be distinguished by the three variables that quantified different aspects of *Iba1+* processes but not by the number of *Iba1+* microglial cells abutting each *GAD67+* neuron. This may reflect the highly motile and dynamic nature of microglial processes, even under quiescent conditions (Wake et al., 2009). Other features of GABAergic neurons in IC, such as their discharge patterns and expression of associated ion channels also do not relate to soma size (Ono et al., 2005). Interestingly, the two newly identified clusters of *GAD67+* neurons did not differ in their relative proportion between the four sub-regions in IC. Future work may investigate the differing afferent neural inputs to and efferent target of these cells, to identify likely physiological and connectional differences between clusters and their relationship to GABAergic signaling in auditory processing.

Technical Considerations

The use of primary antibodies in less studied species such as guinea pig can be challenging due to potential differences in epitopes and when not adequately controlled for, this may lead to spurious observations (Schonbrunn, 2014). This is particularly important when using exploratory approaches such as in the present study, to ensure all analyses are predicated on specific and selective labelling (Voskuil, 2017). We therefore conducted extensive control experiments, excluding primary antibody only, secondary antibody only and both antibodies,

as well as changing mounting media and solutions throughout optimization of labelling, to ensure that analyses were based on true labelling.

The lack of *GFAP+* astrocytes in IC parenchyma was surprising and necessitated numerous confirmatory experiments. However, in all cases, a lack of *GFAP+* astrocytes in the parenchyma was found alongside extensive labelling in *peri*-vascular regions and the *glia limitans externa*, demonstrating consistency within and between cases. The lack of *GFAP+* astrocytes in IC parenchyma does not exclude the possibility that astrocytes reside throughout IC. Indeed, a recent report employing SR101 as a marker revealed a network of putative astrocytes throughout CNIC (Ghirardini et al., 2018). However, there is some labelling of oligodendrocytes with this marker, which hampers interpretability in studies trying to selectively label astrocytes (Hill and Grutzendler, 2014). Functional differences between astrocytes in CNIC and the outer layers of DCIC and LCIC have been suggested previously via 3-chloropropanediol-induced lesions, which selectively destroyed the former but not the latter (Willis et al., 2003; Willis et al., 2004). The present study leads to the speculation of fundamental gliochemical and physiological differences that may relate to the sub-region specific roles astrocytes and microglia play in their local milieux (Lawson et al., 1990; Olah et al., 2011). Recently, RT-PCR of single IC astrocytes revealed expression of functional inhibitory neurotransmitter transporters *GlyT1*, *GAT-1*, and *GAT-3* (Ghirardini et al., 2018). Sub-regional differences in *GAD67+* neurons in the present study suggest that GABAergic and glycinergic signaling released from and received by glial cells may also exhibit such variations throughout IC and perhaps in other structures.

Colocalization of *synaptophysin* and *Iba1* with *homer1* does not guarantee that this labelling is representative of neuron-neuron chemical synapses. *Homer1* has been shown to localize with metabotropic glutamate receptors on astrocytes (Buscemi et al., 2017). Due to the absence of parenchymal *GFAP* labelling in the present study, we can exclude these astrocytes as potential *loci* of *homer1+* labelling, but we cannot rule out non-*GFAP* expressing astrocytes. As astrocytes are known to interact at synapses, this would not exclude the possibility of functional neuron-neuron chemical synapses being identified using this approach. However, the strong weight of probability is that many of the observed *loci* of colocalization between *synaptophysin*, *Iba1,* and *homer1* are chemical synapses between neurons, closely abutted by microglial processes.

Conclusions

There is a wealth of literature that has explored the electrophysiological nature of neurons in sensory systems, but our knowledge of glial cells lags far behind. We have shown that *Iba1+* microglia, but not *GFAP+* astrocytes, colocalize at synapses throughout IC, with a greater number in DCIC, a sub-region specialized to mediate top-down plasticity. Furthermore, we discovered two new clusters of *GAD67+* neurons which can be distinguished based on the total amount of *Iba1+* contacts they receive. These data highlight the fundamental role microglia play in the organization and likely function of sensory systems in the healthy mature brain.

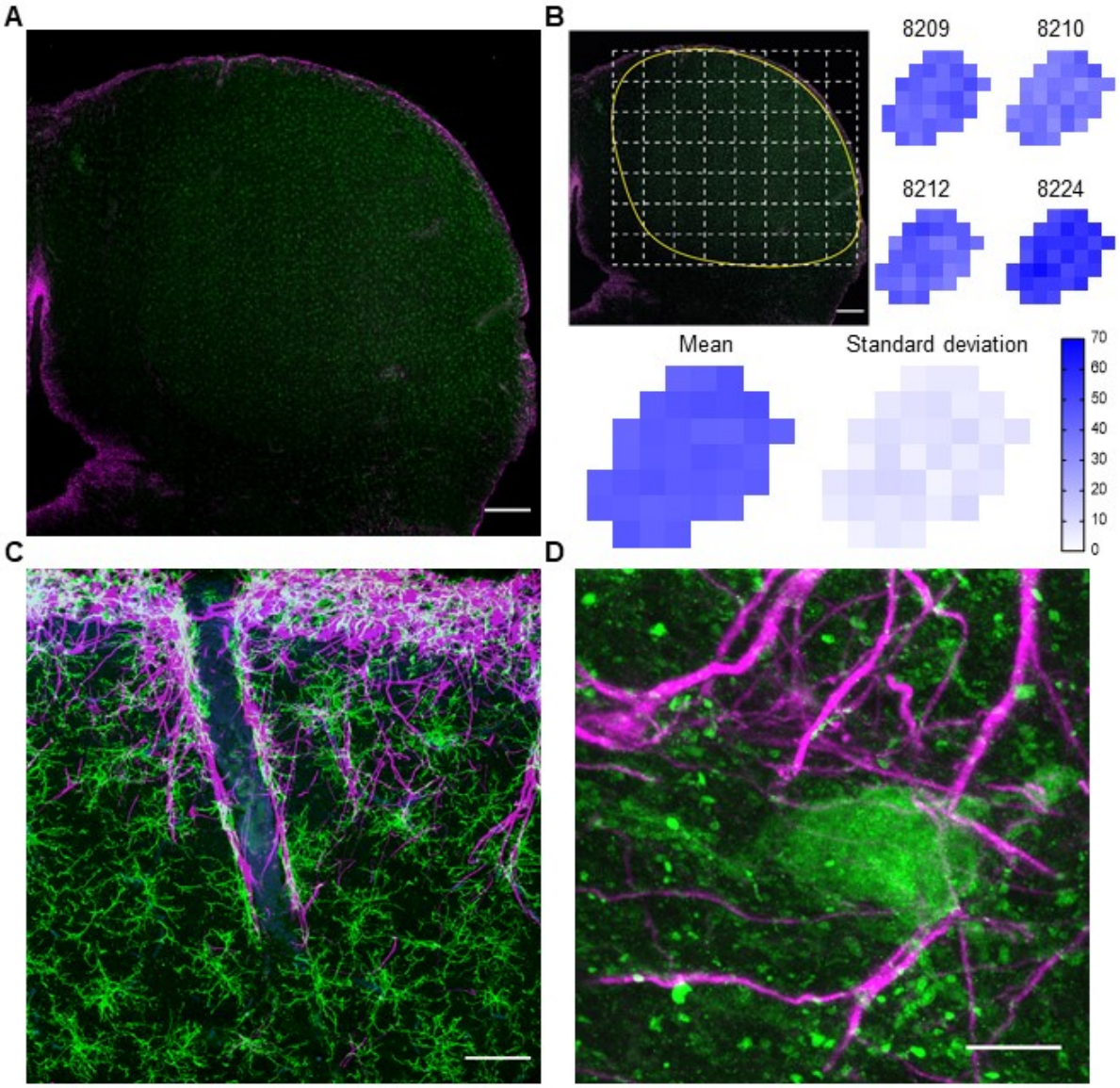

Figure 1. Microglia and astrocytes form the *glia limitans externa* and *peri*-vascular borders but only microglia tile the parenchyma. (A) Tiled maximum intensity projection confocal micrograph of *GFAP+* astrocytes (magenta) and *Iba1*$^{+}$ microglia (green) in IC. Scale bar 400µm. Note that *GFAP* labelling is restricted to the peripheral borders and penetrating vessels while *Iba1* is evenly distributed throughout. (B) Quantification of *Iba1+* somata counts per 450µm^2 grid within the parenchyma across all four cases. Numbers on top row refer to individual animals. (C) Confocal micrograph showing *GFAP, Iba1* and *GSL1* (blue) labelling of a penetrating arteriole coursing into IC. Scale bar 50µm. (D) Confocal micrograph showing a *calbindin* (green) expressing neuron in the outer layers of the LCIC surrounded by *GFAP+* axo-somatic processes. Scale bar 10µm.

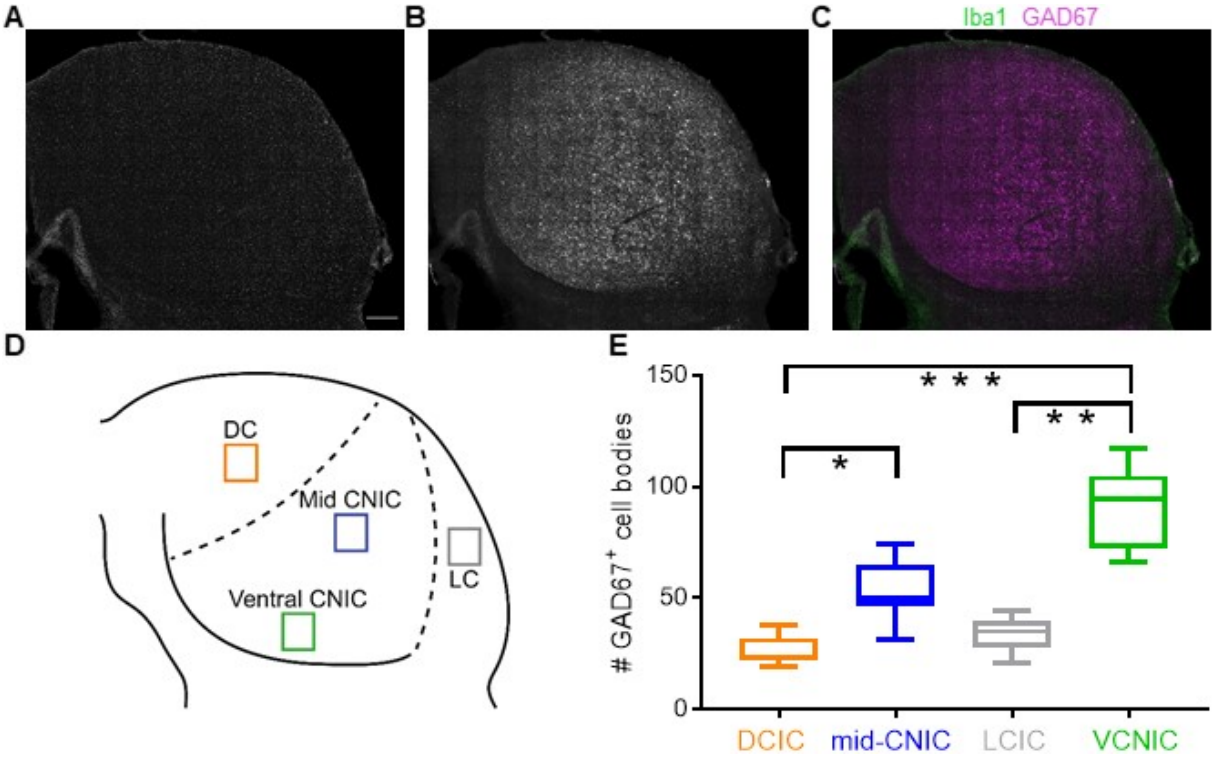

Figure 2. *GAD67+* neurons vary in density between sub-regions of IC. (A) Tiled confocal micrograph showing *Iba1+* microglia tiling IC parenchyma. Scale bar 400µm (same for B and C). (B) *GAD67+* neuropil can be seen to demark the medial and ventral borders of the IC. *GAD67+* neurons are found throughout IC but vary in density. (C) Merge of A (green) and B (magenta). (D) Borders of IC sub-regions were delineated using those defined by Coote and Rees (2008). ROIs were located within distinct sub-regions of IC that could be clearly distinguished from one another. (E) Box plot showing *GAD67+* somata counts in each sub-region of interest, across cases. The VCNIC consistently had the highest number of *GAD67+* somata while numbers in DCIC and LCIC were lower than mid-CNIC.

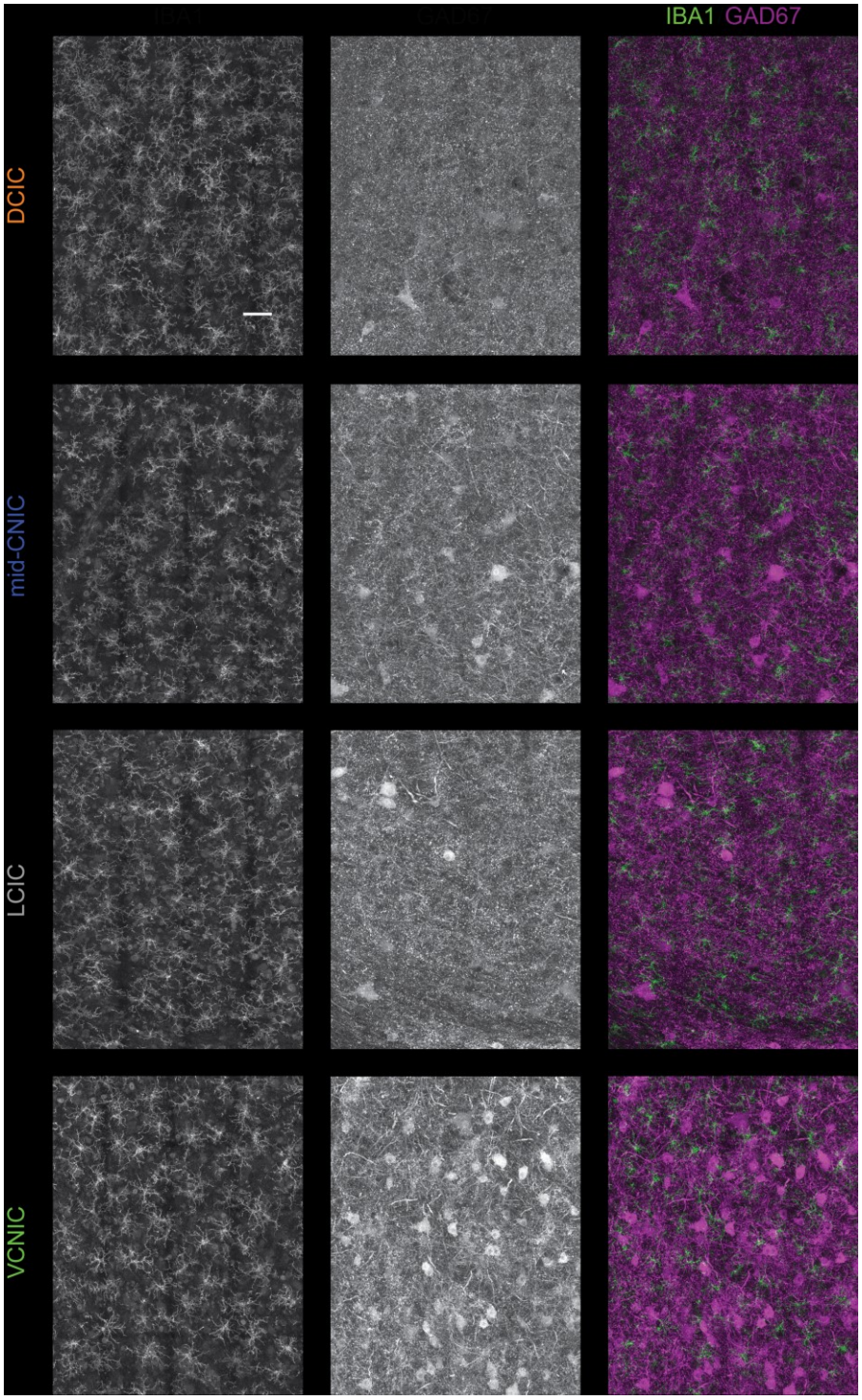

Figure 3. Representative ROI panoramas show differences between *Iba1+* and *GAD67+* cells in sub-regions of IC. Scale bar in (A) 50µm. Same scale for all panels. Maximum intensity projections of tiled confocal panoramas in all sub-regions show (left column; A-D) *Iba1+* microglia tiling the parenchyma with similar density. Conversely, labelling of *GAD67+* somata (middle column, E-H) reveals varied cell densities between sub-regions. Merging both labels (right column; I-L) reveals intercalating of *Iba1+* processes with *GAD67+* labelling.

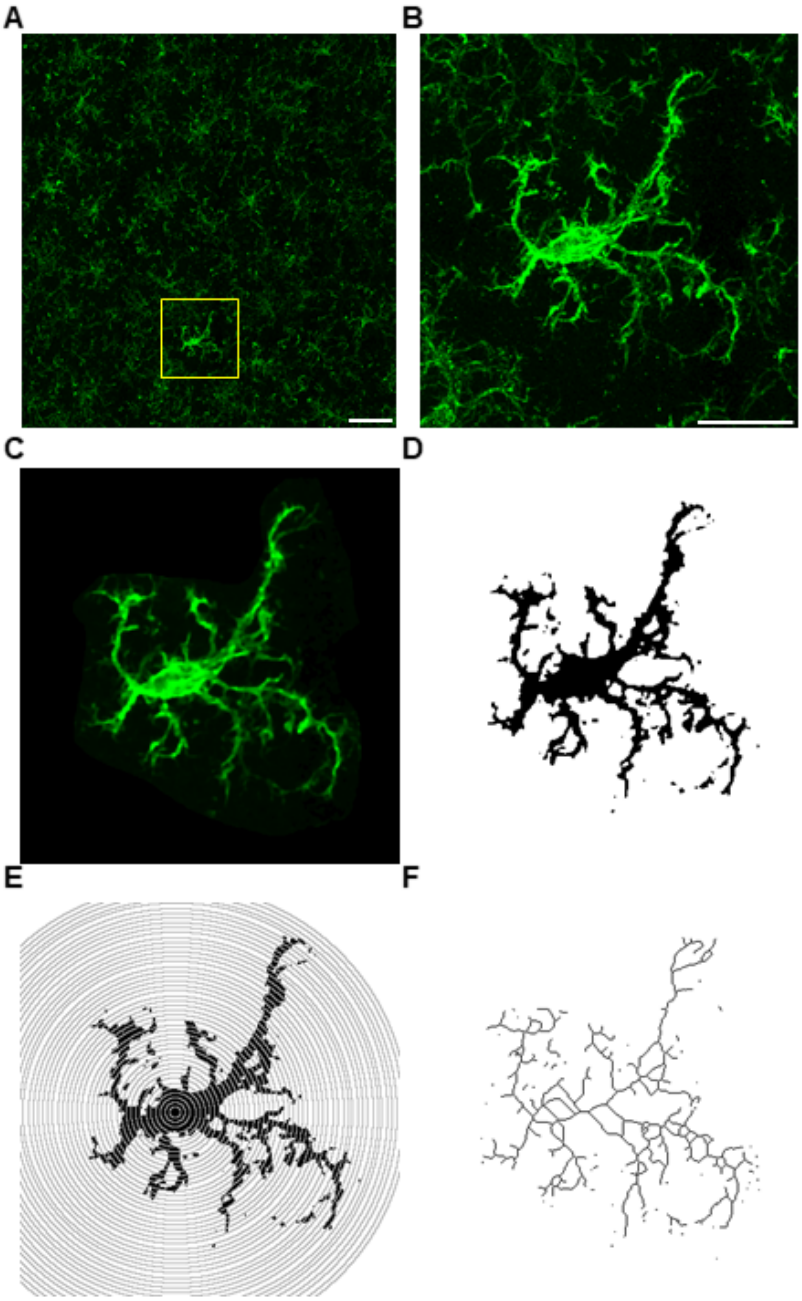

Figure 4. Process for Sholl analyses to quantify morphological characteristics of *Iba1+* microglia. (A) Example of maximum intensity projection of ROI tiled confocal micrographs showing *Iba1+* microglia in IC. A 6-column x 5-row field of view tiled image was taken using 0.99µm z-slices. Individual cells were subject to Sholl analysis (yellow box inset). Scale bar 50µm. (B) Extracted cell from (A) showing high resolution imaging of soma and processes surrounded by non-cellular labelling. Scale bar 20µm. Same scale bar for panels C-F. (C) Non-cellular labelling was cropped and (D) thresholded to binarize cellular processes. (E) Sholl analyses were performed at 1µm resolution from binarized images. (F) Skeletonized cell framework from (D) to be analyzed for number of branches and max branch length.

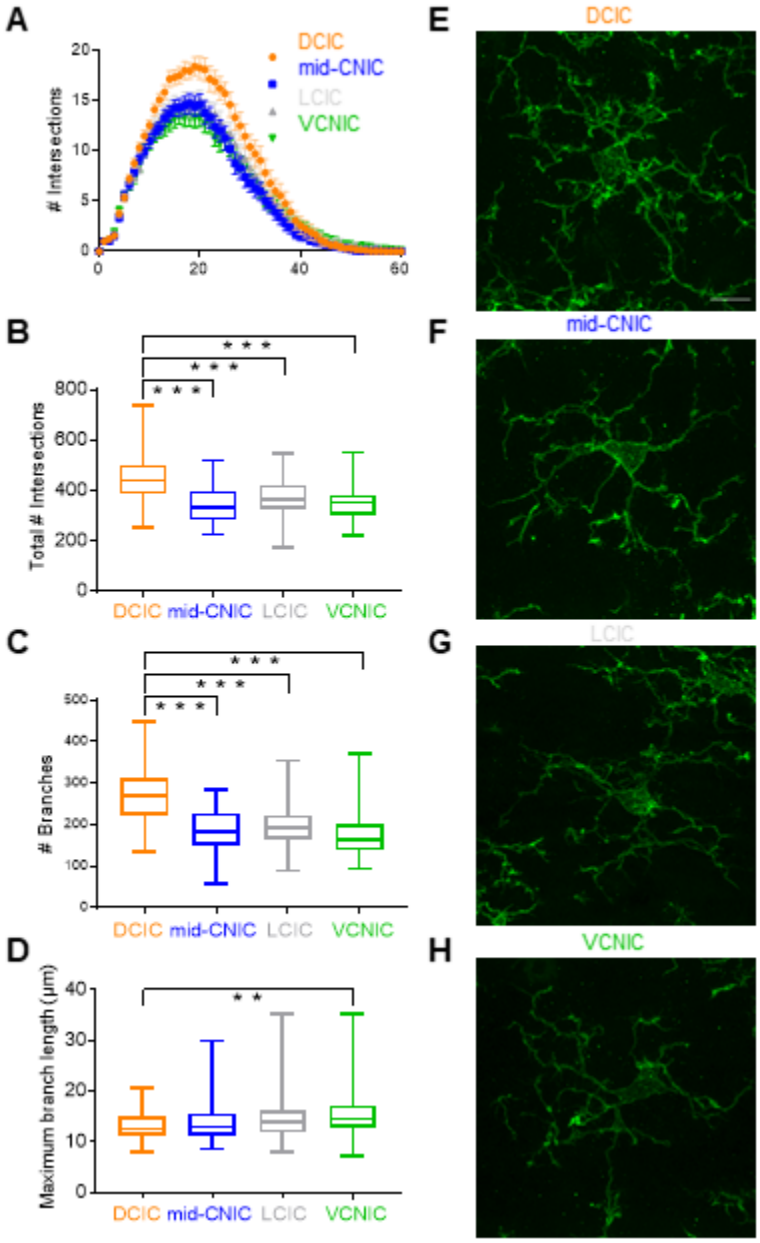

Figure 5. *Iba1+* microglia are more ramified in DCIC than other sub-regions of IC. (A) Sholl analyses (mean ±95% confidence intervals) showing *Iba1+* microglia in DCIC have greater numbers of ramifications than other IC sub-regions at all distances from the soma. (B) Total number of ramification intersections independent of distance from soma are greater in DCIC. (C) Greater number of intersections in DCIC are due to a greater number of branching ramifications. (D) Maximum branch length, a measure of how long ramifications travel before branching, are longest in VCNIC and shortest in DCIC. Representative examples of *Iba1+* microglia in (E) DCIC, (F) mid-CNIC, (G) LCIC and (H) VCNIC. Scale bar 10µm. Same scale bar for F-H.

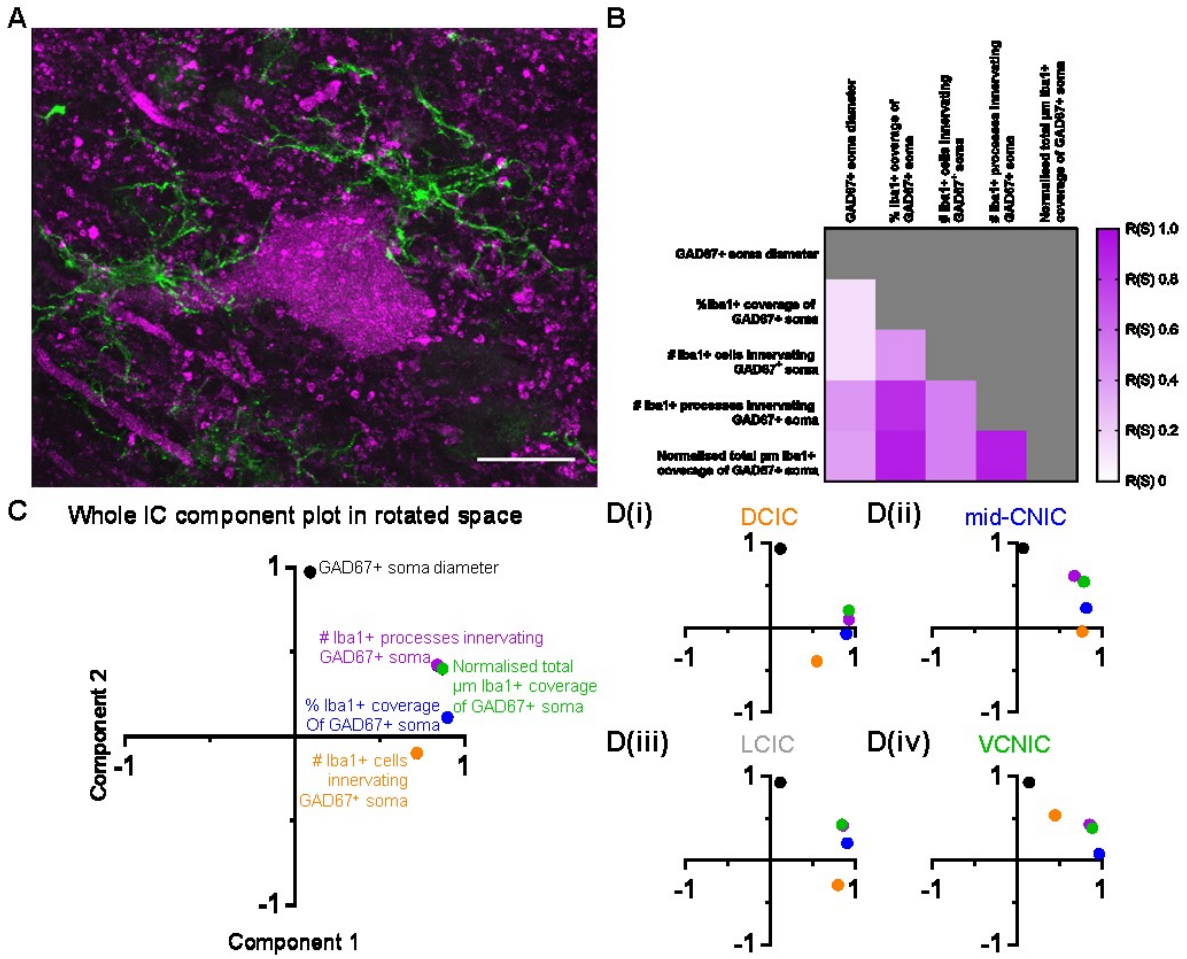

Figure 6. (A) Representative *GAD67+* cell (magenta) receiving abutting somatic processes from two *Iba1+* microglia (green). Scale bar 20µm. (B) Correlation matrix showing Spearman's rank correlation coefficient for each combination of measures derived from putative interactions between *Iba1+* microglia and *GAD67+* cells. Note lower values in first column. (C) Principal component analysis of the five variables in (B). *GAD67+* soma diameter separated from the other four variables, which grouped together. (D) As (C) but for each sub-region in IC, showing similar findings in all sub-regions, suggesting robust clustering throughout IC.

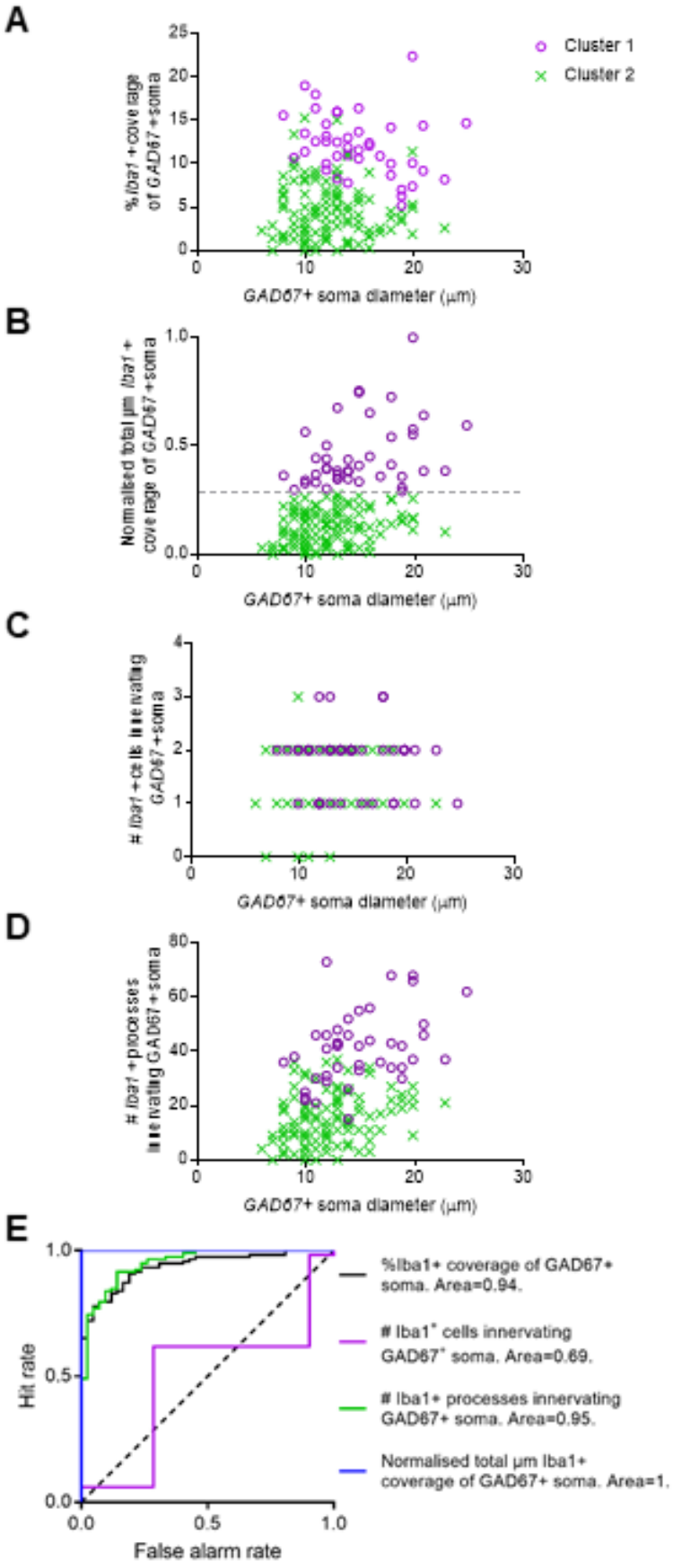

606

607 **Figure 7.** *GAD67+* neurons in IC can be classified into two clusters based on the amount of
608 somatic *Iba1+* contacts they receive. Scatterplots showing each *GAD67+* cell (n=160) from
609 the cluster analysis, classified into either cluster 1 (magenta open circle; n=42) or cluster 2
610 (green crosses; n=118) for each *Iba1+* related variable, plotted as a function of *GAD67+* soma
611 diameter: (A) Percentage *Iba1+* coverage of *GAD67+* soma; (B) normalized total µm *Iba1+*
612 coverage of *GAD67+* soma; (C) number of *Iba1+* cells abutting *GAD67+* soma; (D) number of
613 *Iba1+* processes abutting *GAD67+* soma. (E) ROC analyses showing classifier performance of
614 each variable in discriminating *GAD67+* cells into cluster 1 or cluster 2. Normalized total µm
615 *Iba1+* coverage of *GAD67+* soma could perfectly classify *GAD67+* cells using a cut-off value
616 of 0.28.

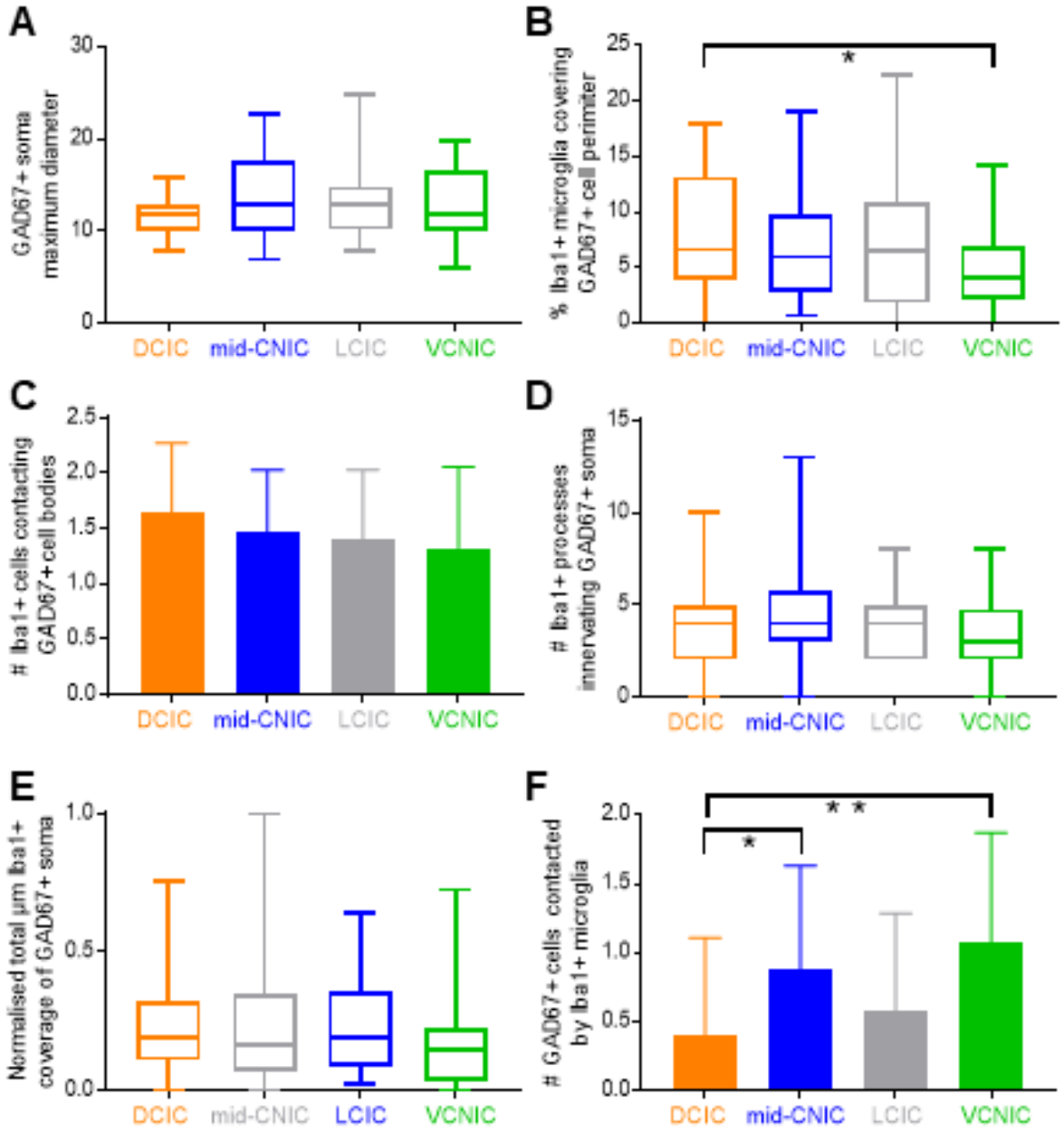

Figure 8. No clear relationship between measured variables and IC sub-region. (A) *GAD67+* soma diameter was similar across sub-regions of IC. (B) The percentage of *Iba1+* coverage of *GAD67+* somata was lower in VCNIC than the other three sub-regions. (C) The number of *Iba1+* cells contacting *GAD67+* somata, (D) the number of *Iba1+* processes abutting *GAD67+* somata, and (E) the normalized total µm of *Iba1+* coverage of *GAD67+* somata did not differ between sub-regions. (F) There were, on average, a greater number of *GAD67+* somata contacted by each *Iba1+* cell, owing to the greater density of *GAD67+* cells in VCNIC.

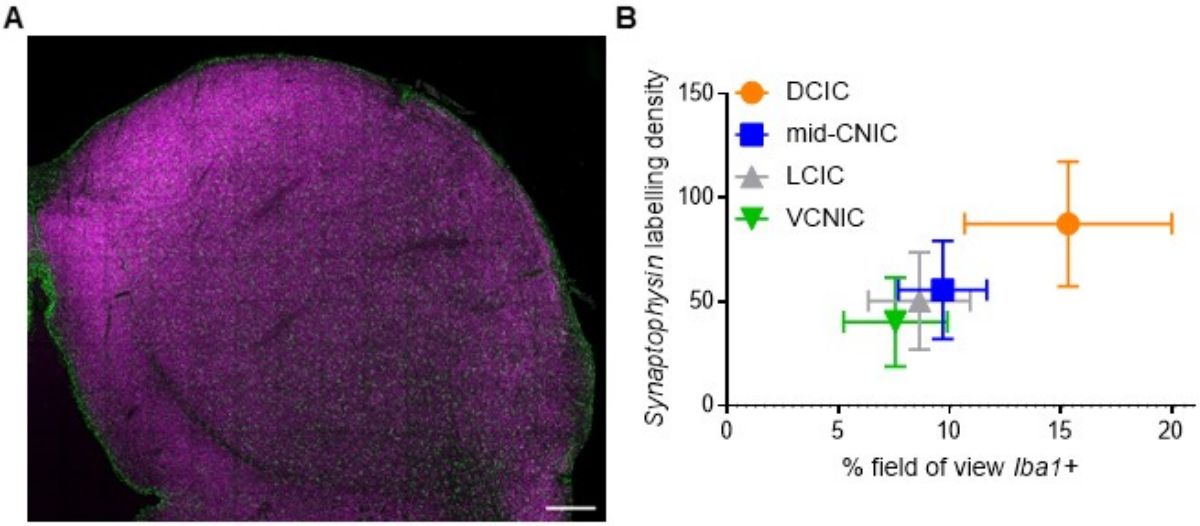

Figure 9. Presynaptic marker *synaptophysin* has greater density of labelling in DCIC and correlates with *Iba1* labelling. (A) Tiled confocal micrograph showing representative *synaptophysin* (magenta) and *Iba1* (green) labelling. Note the greater density of *synaptophysin* labelling in DCIC. Scale bar 400µm (B) Quantification from ROIs in sub-regions showing greater *synaptophysin* puncta density in DCIC which correlates with *Iba1* percentage field of view labelling.

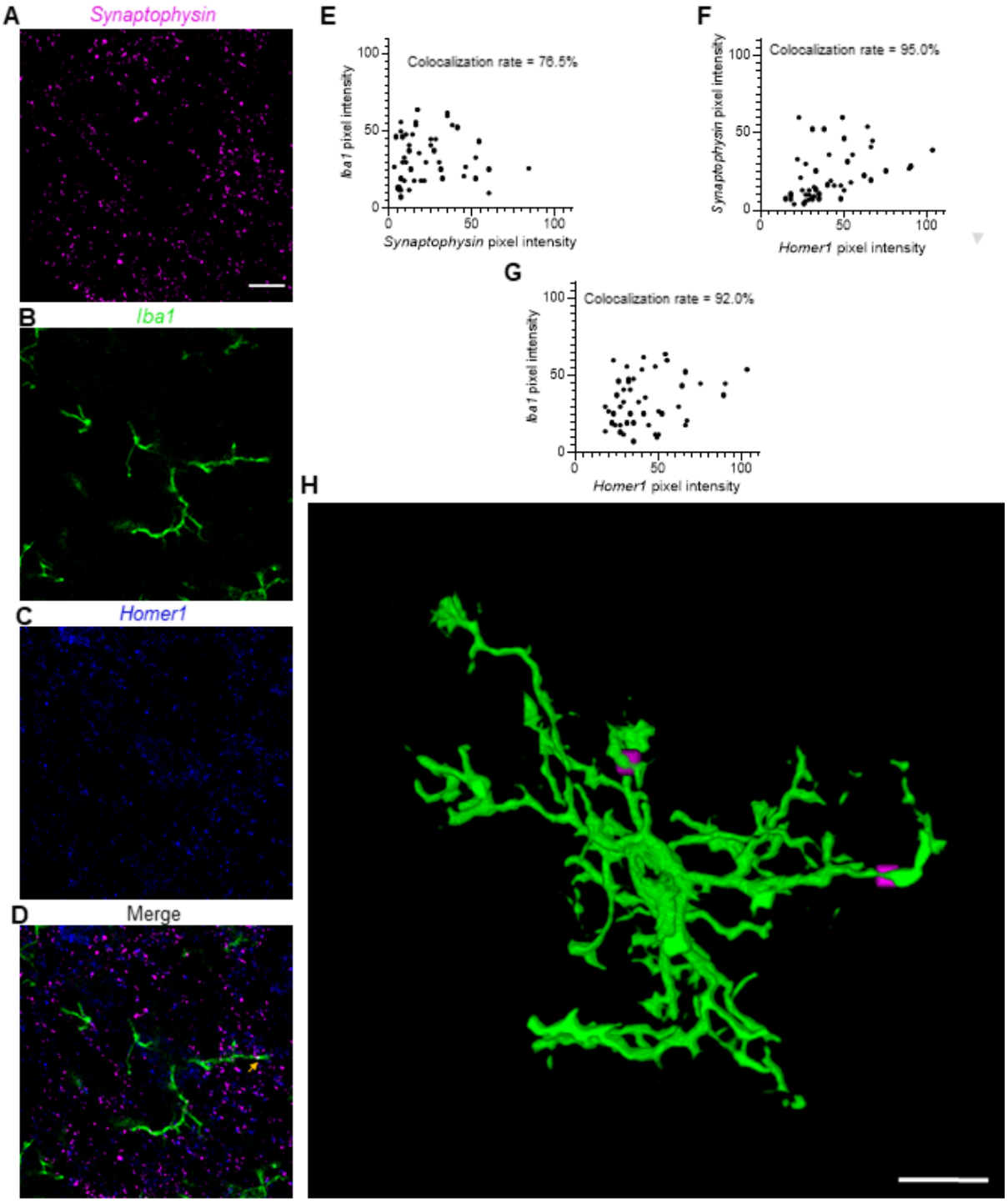

Figure 10. Colocalization of *synaptophysin* and *homer1* on 3D reconstructed *Iba1+* microglia. Single plane confocal micrograph showing (A) *synaptophysin*, (B) *Iba1*, (C) *homer1* and (D) merged image. Arrowhead shows point of colocalization of all three labels. All z-planes were thresholded, binarized and pixels containing positive labelling for all three channels were quantified. Scale bar 10µm. ROI analysis of points of colcalization showing pixel intensity for (E) *synaptophysin* and *Iba1*, (F) *synaptophysin* and *homer1* and (G) *Iba1* and *homer1*. All combinations showed high rates of colocalization within ROI. (H) 3D reconstruction of *Iba1+*

640 microglial cell in VCNIC (green, as in B) showing two points of *synaptophysin+* and *homer1+*
641 colocalization (magenta; as in A and C, respectively). Green signal to scale in (D) 10µm,
642 magenta points of colocalization have been made 13-fold larger for clarity.

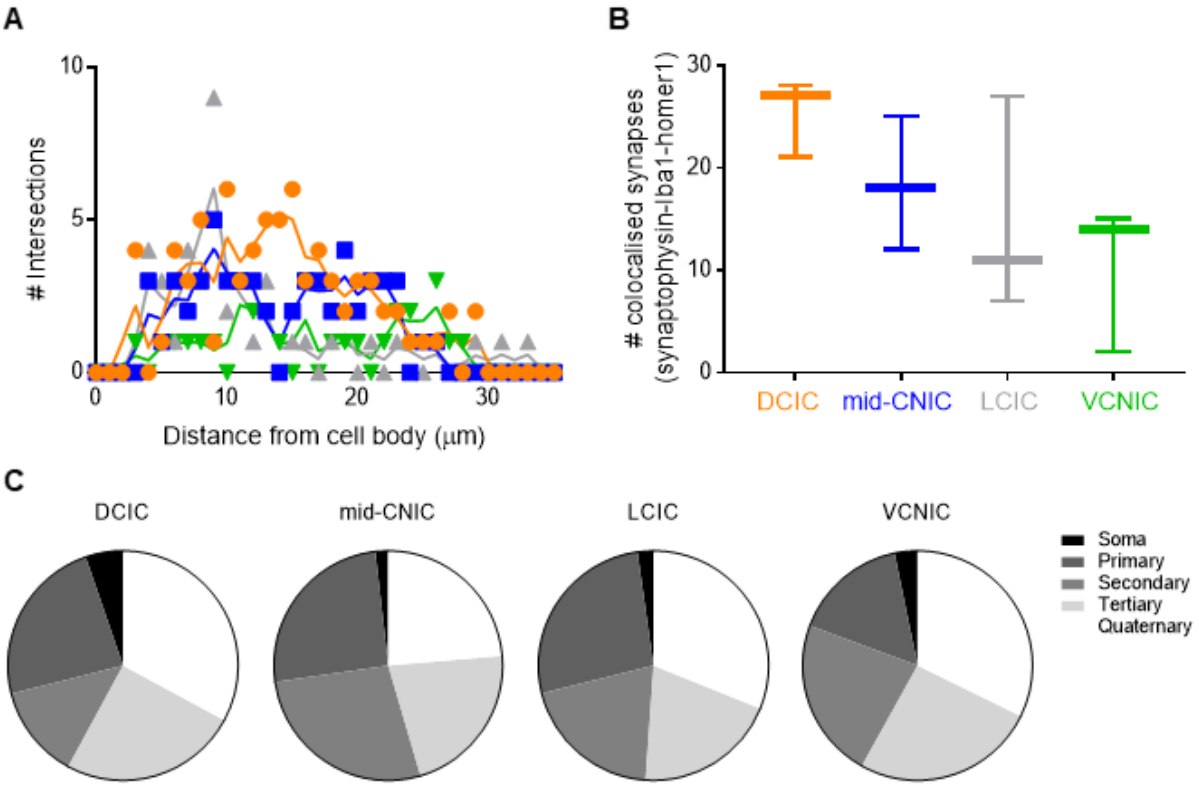

643

644 **Figure 11.** *Iba1* colocalizes at *synaptophysin+* and *homer1+* puncta in greater numbers in
645 DCIC. (A) 3D volume Sholl analysis (plotted in 2D) showing colocalization of *synaptophysin+*
646 and *homer1+* puncta on *Iba1+* microglia (n=3 per sub-region, colour-coded as in B). LOWESS
647 regressions highlight greater values in DCIC. (B) Number of colocalized puncta per microglia.
648 The DCIC had a greater number of puncta per microglia. (E) Analyses of puncta location on
649 *Iba1+* branched ramifications show few puncta are located on somata and similar proportions
650 are found on primary, secondary, tertiary and quaternary branches across sub-regions.

Sub-region	Soma	Primary	Secondary	Tertiary	Quaternary
DCIC	4 (5.3)	18 (23.7)	10 (13.2)	19 (25)	25 (32.9)
mid-CNIC	1 (1.8)	14 (25.5)	15 (27.3)	12 (21.8)	13 (23.6)
LCIC	1 (2.2)	12 (26.7)	9 (20)	9 (20)	14 (31.1)
VCNIC	1 (3.2)	5 (16.1)	7 (22.6)	8 (25.8)	10 (32.2)

651

652 **Table 1.** Absolute numbers (and % of the total for that sub-region) of colocalized puncta
653 positive for *synaptophysin*, *Iba1* and *homer1*, as shown in Figure 11C. Note similar proportions
654 of puncta both within and between sub-regions.

655 ## References

656 Abràmoff MD, Magalhães PJ, Ram SJ (2004) Image processing with ImageJ. Biophotonics
657 International 11:36-42.

658 Aitkin LM, Dickhaus H, Schult W, Zimmermann M (1978) External nucleus of inferior colliculus
659 - auditory and spinal somatosensory afferents and their interactions. Journal of
660 Neurophysiology 41:837-847.

661 Ayala Y, Malmierca M (2013) Stimulus-specific adaptation and deviance detection in the
662 inferior colliculus. Frontiers in Neural Circuits 6:89.

663 Bajo VM, Moore DR (2005) Descending projections from the auditory cortex to the inferior
664 colliculus in the gerbil, Meriones unguiculatus. Journal of Comparative Neurology
665 486:101-116.

666 Bajo VM, Nodal FR, Moore DR, King AJ (2010) The descending corticocollicular pathway
667 mediates learning-induced auditory plasticity. Nature Neuroscience 13:253-260.

668 Bajo VM, Nodal FR, Bizley JK, Moore DR, King AJ (2006) The ferret auditory cortex: descending
669 projections to the inferior colliculus. Cerebral Cortex 17:475-491.

670 Baumann S, Griffiths TD, Sun L, Petkov CI, Thiele A, Rees A (2011) Orthogonal representation
671 of sound dimensions in the primate midbrain. Nature Neuroscience 14:423-425.

672 Beebe NL, Young JW, Mellott JG, Schofield BR (2016) Extracellular molecular markers and soma
673 size of inhibitory neurons: evidence for four subtypes of GABAergic cells in the inferior
674 colliculus. Journal of Neuroscience 36:3988-3999.

675 Brakeman PR, Lanahan AA, O'Brien R, Roche K, Barnes CA, Huganir RL, Worley PF (1997)
676 Homer: A protein that selectively binds metabotropic glutamate receptors. Nature
677 386:284-288.

678 Bulloch K, Miller MM, Gal-Toth J, Milner TA, Gottfried-Blackmore A, Waters EM, Kaunzner UW,
679 Liu K, Lindquist R, Nussenzweig MC, Steinman RM, McEwen BS (2008) CD11c/EYFP
680 transgene illuminates a discrete network of dendritic cells within the embryonic,
681 neonatal, adult, and injured mouse brain. Journal of Comparative Neurology 508:687-
682 710.

683 Buscemi L, Ginet V, Lopatar J, Montana V, Pucci L, Spagnuolo P, Zehnder T, Grubišić V, Truttman
684 A, Sala C, Hirt L, Parpura V, Puyal J, Bezzi P (2017) Homer1 scaffold proteins govern
685 Ca2+ dynamics in normal and reactive astrocytes. Cerebral Cortex 27:2365-2384.
686 Ciruela F, Soloviev MM, Chan WY, McIlhinney RA (2000) Homer-1c/Vesl-1L modulates the cell
687 surface targeting of metabotropic glutamate receptor type 1alpha: evidence for an
688 anchoring function. Molecular and Cellular Neuroscience 15:36-50.
689 Clifton NE, Cameron D, Trent S, Sykes LH, Thomas KL, Hall J (2017) Hippocampal regulation of
690 postsynaptic density homer1 by associative learning. Neural Plasticity 2017:11.
691 Coote EJ, Rees A (2008) The distribution of nitric oxide synthase in the inferior colliculus of
692 guinea pig. Neuroscience 154:218-225.
693 De Martino F, Moerel M, van de Moortele PF, Ugurbil K, Goebel R, Yacoub E, Formisano E
694 (2013) Spatial organization of frequency preference and selectivity in the human
695 inferior colliculus. Nature Communications 4:1386.
696 Debus E, Weber K, Osborn M (1983) Monoclonal-antibodies specific for glial fibrillary acidic
697 (GFA) protein and for each of the neurofilament triplet polypeptides. Differentiation
698 25:193-203.
699 Engle JR, Gray DT, Turner H, Udell JB, Recanzone GH (2014) Age-related neurochemical
700 changes in the rhesus macaque inferior colliculus. Frontiers in Aging Neuroscience 6:73.
701 Faye-Lund H, Osen KK (1985) Anatomy of the inferior colliculus in rat. Anatomy and
702 Embryology 171:1-20.
703 Feliciano M, Potashner SJ (1995) Evidence for a glutamatergic pathway from the guinea-pig
704 auditory-cortex to the inferior colliculus. Journal of Neurochemistry 65:1348-1357.
705 Fong AY, Stornetta RL, Foley CM, Potts JT (2005) Immunohistochemical localization of GAD67-
706 expressing neurons and processes in the rat brainstem: subregional distribution in the
707 nucleus tractus solitarius. Journal of Comparative Neurology 493:274-290.
708 Foster NL, Mellott JG, Schofield BR (2014) Perineuronal nets and GABAergic cells in the inferior
709 colliculus of guinea pigs. Frontiers in Neuroanatomy 7:53.
710 Freund TF, Buzsaki G (1996) Interneurons of the hippocampus. Hippocampus 6:347-470.
711 Fuentes-Santamaría V, Alvarado JC, Juiz JM (2012) Long-term interaction between microglial
712 cells and cochlear nucleus neurons after bilateral cochlear ablation. Journal of
713 Comparative Neurology 520:2974-2990.

714 Games KD, Winer JA (1988) Layer V in rat auditory: cortex projections to the inferior colliculus
715 and contralateral cortex. Hearing Research 34:1-26.
716 Gavrilovici C, D'Alfonso S, Poulter MO (2010) Diverse interneuron populations have highly
717 specific interconnectivity in the rat piriform cortex. Journal of Comparative Neurology
718 518:1570-1588.
719 Geis HRAP, Borst JGG (2013) Intracellular responses to frequency modulated tones in the
720 dorsal cortex of the mouse inferior colliculus. Frontiers in Neural Circuits 7:7.
721 Ghirardini E, Wadle SL, Augustin V, Becker J, Brill S, Hammerich J, Seifert G, Stephan J (2018)
722 Expression of functional inhibitory neurotransmitter transporters GlyT1, GAT-1, and
723 GAT-3 by astrocytes of inferior colliculus and hippocampus. Molecular Brain 11:4.
724 Gimse K, Gorzek RC, Olin A, Osting S, Burger C (2018) Hippocampal Homer1b/c is necessary
725 for contextual fear conditioning and group I metabotropic glutamate receptor
726 mediated long-term depression. Neurobiology of Learning and Memory 156:17-23.
727 Gleich O, Netz J, Strutz J (2014) Comparing the inferior colliculus of young and old gerbils
728 (Meriones unguiculatus) with an emphasis on GABA. Experimental Gerontology 57:155-
729 162.
730 Glueckert R, Bitsche M, Miller JM, Zhu YY, Prieskorn DM, Altschuler RA, Schrott-Fischer A (2008)
731 Deafferentiation-associated changes in afferent and efferent processes in the guinea
732 pig cochlea and afferent regeneration with chronic intrascalar brain-derived
733 neurotrophic factor and acidic fibroblast growth factor. Journal of Comparative
734 Neurology 507:1602-1621.
735 Goodings L, He J, Wood AJ, Harris WA, Currie PD, Jusuf PR (2017) In vivo expression of
736 Nurr1/Nr4a2a in developing retinal amacrine subtypes in zebrafish Tg(nr4a2a:eGFP)
737 transgenics. Journal of Comparative Neurology 525:1962-1979.
738 Hayashi Y, Ishibashi H, Hashimoto K, Nakanishi H (2006) Potentiation of the NMDA receptor-
739 mediated responses through the activation of the glycine site by microglia secreting
740 soluble factors. Glia 53:660-668.
741 Helfer JL, Goodlett CR, Greenough WT, Klintsova AY (2009) The effects of exercise on
742 adolescent hippocampal neurogenesis in a rat model of binge alcohol exposure during
743 the brain growth spurt. Brain Research 1294:1-11.

744 Herbert H, Aschoff A, Ostwald J (1991) Topography of projections from the auditory cortex to
745 the inferior colliculus in the rat. Journal of Comparative Neurology 304:103-122.
746 Hill RA, Grutzendler J (2014) In vivo imaging of oligodendrocytes with sulforhodamine 101.
747 Nature Methods 11:1081-1082.
748 Huynh DP, Figueroa K, Hoang N, Pulst SM (2000) Nuclear localization or inclusion body
749 formation of ataxin-2 are not necessary for SCA2 pathogenesis in mouse or human.
750 Nature Genetics 26:44-50.
751 Imai Y, Ibata I, Ito D, Ohsawa K, Kohsaka S (1996) A novel gene iba1 in the major
752 histocompatibility complex class III region encoding an EF hand protein expressed in a
753 monocytic lineage. Biochemical and Biophysical Research Communications 224:855-
754 862.
755 Ito T, Bishop DC, Oliver DL (2009) Two classes of GABAergic neurons in the inferior colliculus.
756 Journal of Neuroscience 29:13860-13869.
757 Jaafari N, Khomitch-Baud A, Gilhodes JC, Hua G, Julé Y (2008) Qualitative and quantitative
758 analysis of tachykinin NK2 receptors in chemically defined human colonic neuronal
759 pathways. Journal of Comparative Neurology 507:1542-1558.
760 Kaas JH, Hackett TA (1999) 'What' and 'where' processing in auditory cortex. Nature
761 Neuroscience 2:1045-1047.
762 Keating P, Dahmen JC, King AJ (2013) Context-specific reweighting of auditory spatial cues
763 following altered experience during development. Current Biology 23:1291-1299.
764 Kelleher MA, Hirst JJ, Palliser HK (2013) Changes in neuroactive steroid concentrations after
765 preterm delivery in the guinea pig. Reproductive Sciences 20:1365-1375.
766 Kelleher MA, Palliser HK, Walker DW, Hirst JJ (2011) Sex-dependent effect of a low neurosteroid
767 environment and intrauterine growth restriction on foetal guinea pig brain
768 development. Journal of Endocrinology 208:301-309.
769 Knabe W, Washausen S, Happel N, Kuhn HJ (2008) Diversity in mammalian chiasmatic
770 architecture: ipsilateral axons are deflected at glial arches in the prechiasmatic optic
771 nerve of the eutherian Tupaia belangeri. Journal of Comparative Neurology 508:437-
772 457.
773 Komitova M, Zhao LR, Gidö G, Johansson BB, Eriksson P (2005) Postischemic exercise
774 attenuates whereas enriched environment has certain enhancing effects on lesion-

induced subventricular zone activation in the adult rat. European Journal of Neuroscience 21:2397-2405.

Kotani T, Murata Y, Ohnishi H, Mori M, Kusakari S, Saito Y, Okazawa H, Bixby JL, Matozaki T (2010) Expression of PTPRO in the interneurons of adult mouse olfactory bulb. Journal of Comparative Neurology 518:119-136.

Kotti TJ, Ramirez DMO, Pfeiffer BE, Huber KM, Russell DW (2006) Brain cholesterol turnover required for geranylgeraniol production and learning in mice. Proceedings of the National Academy of Sciences of the United States of America 103:3869-3874.

Kumpik DP, King AJ (2019) A review of the effects of unilateral hearing loss on spatial hearing. Hearing Research 372:17-28.

Latov N, Nilaver G, Zimmerman EA, Johnson WG, Silverman AJ, Defendini R, Cote L (1979) Fibrillary astrocytes proliferate in response to brain injury - study combining immunoperoxidase technique for glial fibrillary acidic protein and autoradiography of tritiated-thymidine. Developmental Biology 72:381-384.

Lawson LJ, Perry VH, Dri P, Gordon S (1990) Heterogeneity in the distribution and morphology of microglia in the normal adult-mouse brain. Neuroscience 39:151-170.

Lee JE, Ahn CH, Lee JY, Chung ES, Jeon CJ (2004) Nitric oxide synthase and calcium-binding protein-containing neurons in the hamster visual cortex. Molecules and Cells 18:30-39.

Lee KS, Vandemark K, Mezey D, Shultz N, Fitzpatrick D (2019) Functional synaptic architecture of callosal inputs in mouse primary visual cortex. Neuron 101:421-428 e425.

Lennerz JK, Rühle V, Ceppa EP, Neuhuber WL, Bunnett NW, Grady EF, Messlinger K (2008) Calcitonin receptor-like receptor (CLR), receptor activity-modifying protein 1 (RAMP1), and calcitonin gene-related peptide (CGRP) immunoreactlivity in the rat trigeminovascular system: Differences between peripheral and central CGRP receptor distribution. Journal of Comparative Neurology 507:1277-1299.

Liu S, Gao X, Gao N, Wang X, Fang X, Hu HZ, Wang GD, Xia Y, Wood JD (2005) Expression of type 1 corticotropin-releasing factor receptor in the guinea pig enteric nervous system. Journal of Comparative Neurology 481:284-298.

Lorenz B, Garcia-Segura LM, Doncarlos LL (2005) Cellular phenotype of androgen receptor-immunoreactive nuclei in the developing and adult rat brain. Journal of Comparative Neurology 492:456-468.

806 Malmierca MS, Hackett TA (2010) Structural organization of the ascending auditory pathway.
807 NewYork, NY: Oxford University Press.
808 Merchán M, Aguilar LA, Lopez-Poveda EA, Malmierca MS (2005) The inferior colliculus of the
809 rat: quantitative immunocytochemical study of GABA and glycine. Neuroscience
810 136:907-925.
811 Mouriec K, Balthazart J (2013) Peripubertal proliferation of progenitor cells in the preoptic area
812 of Japanese quail (Coturnix japonica). Brain Research 1516:20-32.
813 Nakamoto KT, Sowick CS, Schofield BR (2013) Auditory cortical axons contact commissural
814 cells throughout the guinea pig inferior colliculus. Hearing Research 306:131-144.
815 Olah M, Biber K, Vinet J, Boddeke HWGM (2011) Microglia phenotype diversity. Cns &
816 Neurological Disorders-Drug Targets 10:108-118.
817 Oliver DL, Winer JA, Beckius GE, Saintmarie RL (1994) Morphology of GABAergic neurons in
818 the inferior colliculus of the cat. Journal of Comparative Neurology 340:27-42.
819 Olthof BMJ, Gartside SE, Rees A (2019) Puncta of neuronal nitric oxide synthase (nNOS)
820 mediate NMDA receptor signaling in the auditory midbrain. Journal of Neuroscience
821 39:876-887.
822 Ono M, Yanagawa Y, Koyano K (2005) GABAergic neurons in inferior colliculus of the GAD67-
823 GFP knock-in mouse: electrophysiological and morphological properties. Neuroscience
824 Research 51:475-492.
825 Orton LD, Papasavvas CA, Rees A (2016) Commissural gain control enhances the midbrain
826 representation of sound location. Journal of Neuroscience 36:4470-4481.
827 Ouda L, Syka J (2012) Immunocytochemical profiles of inferior colliculus neurons in the rat and
828 their changes with aging. Frontiers in Neural Circuits 6:68.
829 Ouda L, Burianova J, Syka J (2012) Age-related changes in calbindin and calretinin
830 immunoreactivity in the central auditory system of the rat. Experimental Gerontology
831 47:497-506.
832 Parks XX, Contini D, Jordan PM, Holt JC (2017) Confirming a role for alpha 9nAChRs and SK
833 potassium channels in type II hair cells of the turtle posterior crista. Frontiers in Cellular
834 Neuroscience 11:356.
835 Pocock JM, Kettenmann H (2007) Neurotransmitter receptors on microglia. Trends in
836 neurosciences 30:527-535.

837 Ramirez DMO, Andersson S, Russell DW (2008) Neuronal expression and subcellular
838 localization of cholesterol 24-hydroxylase in the mouse brain. Journal of Comparative
839 Neurology 507:1676-1693.
840 Reichenbach N, Delekate A, Breithausen B, Keppler K, Poll S, Schulte T, Peter J, Plescher M,
841 Hansen JN, Blank N, Keller A, Fuhrmann M, Henneberger C, Halle A, Petzold GC (2018)
842 P2Y1 receptor blockade normalizes network dysfunction and cognition in an
843 Alzheimer's disease model. Journal of Experimental Medicine 215:1649-1663.
844 Riazi K, Galic MA, Kentner AC, Reid AY, Sharkey KA, Pittman QJ (2015) Microglia-dependent
845 alteration of glutamatergic synaptic transmission and plasticity in the hippocampus
846 during peripheral inflammation. Journal of Neuroscience 35:4942-4952.
847 Roberts RC, Ribak CE (1987a) GABAergic neurons and axon terminals in the brainstem auditory
848 nuclei of the gerbil. Journal of Comparative Neurology 258:267-280.
849 Roberts RC, Ribak CE (1987b) An electron microscopic study of GABAergic neurons and
850 terminals in the central nucleus of the inferior colliculus of the rat. Journal of
851 neurocytology 16:333-345.
852 Rosen RF, Farberg AS, Gearing M, Dooyema J, Long PM, Anderson DC, Davis-Turak J, Coppola
853 G, Geschwind DH, Paré JF, Duong TQ, Hopkins WD, Preuss TM, Walker LC (2008)
854 Tauopathy with paired helical filaments in an aged chimpanzee. Journal of Comparative
855 Neurology 509:259-270.
856 Sala C, Piëch V, Wilson NR, Passafaro M, Liu G, Sheng M (2001) Regulation of dendritic spine
857 morphology and synaptic function by Shank and Homer. Neuron 31:115-130.
858 Sanchez PE, Navarro FP, Fares RP, Nadam J, Georges B, Moulin C, Le Cavorsin M, Bonnet C,
859 Ryvlin P, Belmeguenai A, Bodennec J, Morales A, Bezin L (2009) Erythropoietin receptor
860 expression is concordant with erythropoietin but not with common beta chain
861 expression in the rat brain throughout the life span. Journal of Comparative Neurology
862 514:403-414.
863 Schafer DP, Lehrman EK, Kautzman AG, Koyama R, Mardinly AR, Yamasaki R, Ransohoff RM,
864 Greenberg ME, Barres BA, Stevens B (2012) Microglia sculpt postnatal neural circuits in
865 an activity and complement-dependent manner. Neuron 74:691-705.
866 Schofield BR (2010) Structural organization of the descending auditory pathway. New York,
867 NY: Oxford University Press.

868 Schonbrunn A (2014) Editorial: antibody can get it right: confronting poblems of antibody
869 specificity and irreproducibility. Molecular Endocrinology 28:1403-1407.
870 Sokoloff L, Reivich M, Kennedy C, Des Rosiers MH, Patlak CS, Pettigrew KD, Sakurada O,
871 Shinohara M (1977) The [14C] deoxyglucose method for the measurement of local
872 cerebral glucose utilization: theory, procedure, and normal values in the conscious and
873 anesthetized albino rat. Journal of Neurochemistry 28:897-916.
874 Soloviev MM, Ciruela F, Chan WY, McIlhinney RAJ (2000) Mouse brain and muscle tissues
875 constitutively express high levels of Homer proteins. European Journal of Biochemistry
876 267:634-639.
877 Stanton GB, Kohler SJ, Boklweski J, Cameron JL, Greenough WT (2015) Cytogenesis in the adult
878 monkey motor cortex: perivascular NG2 cells are the major adult born cell type. Journal
879 of Comparative Neurology 523:849-868.
880 Su JM, Gorse K, Ramirez F, Fox MA (2010) Collagen XIX is expressed by interneurons and
881 contributes to the formation of hippocampal synapses. Journal of Comparative
882 Neurology 518:229-253.
883 Sweet RA, Dorph-Petersen KA, Lewis DA (2005) Mapping auditory core, lateral belt, and
884 parabelt cortices in the human superior temporal gyrus. Journal of Comparative
885 Neurology 491:270-289.
886 Syka J, Popelář J, Kvašňák E, Astl J (2000) Response properties of neurons in the central nucleus
887 and external and dorsal cortices of the inferior colliculus in guinea pig. Experimental
888 Brain Research 133:254-266.
889 Toro CT, Hallak JEC, Dunham JS, Deakin JFW (2006) Glial fibrillary acidic protein and glutamine
890 synthetase in subregions of prefrontal cortex in schizophrenia and mood disorder.
891 Neuroscience Letters 404:276-281.
892 Trapp BD, Wujek JR, Criste GA, Jalabi W, Yin X, Kidd GJ, Stohlman S, Ransohoff R (2007)
893 Evidence for synaptic stripping by cortical microglia. Glia 55:360-368.
894 Tremblay MÈ, Lowery RL, Majewska AK (2010) Microglial interactions with synapses are
895 modulated by visual experience. Plos Biology 8:e1000527.
896 Tremblay R, Lee S, Rudy B (2016) GABAergic interneurons in the neocortex: from cellular
897 properties to circuits. Neuron 91:260-292.

898 Tsuda M, Tozaki-Saitoh H, Inoue K (2010) Pain and purinergic signaling. Brain Research
899 Reviews 63:222-232.
900 Voitenko LP, Marlinsky VV (1993) Stereotaxic atlas of the guinea pig brainstem.
901 Neurophysiology 25:52-77.
902 Voskuil JL (2017) The challenges with the validation of research antibodies. F1000Research
903 6:161.
904 Wagner KV, Häusl AS, Pöhlmann ML, Hartmann J, Labermaier C, Müller MB, Schmidt MV (2014)
905 Hippocampal Homer1 levels influence motivational behavior in an operant
906 conditioning task. Plos One 9:e.85975.
907 Wake H, Moorhouse AJ, Jinno S, Kohsaka S, Nabekura J (2009) Resting microglia directly
908 monitor the functional state of synapses in vivo and determine the fate of ischemic
909 terminals. Journal of Neuroscience 29:3974-3980.
910 Watson RE, Wiegand SJ, Clough RW, Hoffman GE (1986) Use of cryoprotectant to maintain
911 long-term peptide immunoreactivity and tissue morphology. Peptides 7:155-159.
912 Wiedenmann B, Franke WW (1985) Identification and localization of synaptophysin, an integral
913 membrane glycoprotein of Mr 38,000 characteristic of presynaptic vesicles. Cell
914 41:1017-1028.
915 Willis CL, Leach L, Clarke GJ, Nolan CC, Ray DE (2004) Reversible disruption of tight junction
916 complexes in the rat blood-brain barrier, following transitory focal astrocyte loss. Glia
917 48:1-13.
918 Willis CL, Nolan CC, Reith SN, Lister T, Prior MJ, Guerin CJ, Mavroudis G, Ray DE (2003) Focal
919 astrocyte loss is followed by microvascular damage, with subsequent repair of the
920 blood-brain barrier in the apparent absence of direct astrocytic contact. Glia 45:325-
921 337.
922 Winer JA, Prieto JJ (2001) Layer V in cat primary auditory cortex (AI): Cellular architecture and
923 identification of projection neurons. Journal of Comparative Neurology 434:379-412.
924 Winer JA, Larue DT, Diehl JJ, Hefti BJ (1998) Auditory cortical projections to the cat inferior
925 colliculus. Journal of Comparative Neurology 400:147-174.
926 Yanpallewar SU, Fernandes K, Marathe SV, Vadodaria KC, Jhaveri D, Rommelfanger K, Ladiwala
927 U, Jha S, Muthig V, Hein L, Bartlett P, Weinshenker D, Vaidya VA (2010) alpha(2)-

928 Adrenoceptor blockade accelerates the neurogenic, neurotrophic, and behavioral
929 effects of chronic antidepressant treatment. Journal of Neuroscience 30:1096-1109.
930 Yu CX, Derdikman D, Haidarliu S, Ahissar E (2006) Parallel thalamic pathways for whisking and
931 touch signals in the rat. Plos Biology 4:e124.
932 Zelano J, Berg A, Thams S, Hailer NP, Cullheim S (2009) SynCAM1 expression correlates with
933 restoration of central synapses on spinal motoneurons after two different models of
934 peripheral nerve injury. Journal of Comparative Neurology 517:670-682.
935 Zettel ML, Frisina RD, Haider SE, O'Neill WE (1997) Age-related changes in calbindin D-28k and
936 calretinin immunoreactivity in the inferior colliculus of CBA/CaJ and C57Bl/6 mice.
937 Journal of Comparative Neurology 386:92-110.
938 Zhang J, Malik A, Choi HB, Ko RW, Dissing-Olesen L, MacVicar BA (2014) Microglial CR3
939 activation triggers long-term synaptic depression in the hippocampus via NADPH
940 oxidase. Neuron 82:195-207.

941